ACS Catalysis
Research Article
pubs.acs.org/acscatalysis

# Probing the Nature of the Active Phase of Molybdenum-Supported Catalysts for the Direct Synthesis of Methylmercaptan from Syngas and $H_2S$

A. Cordova,[†] P. Blanchard,[†] C. Lancelot,[†] G. Frémy,[‡] and C. Lamonier*,[†]

[†]Unité de Catalyse et de Chimie du Solide, CNRS UMR 8181, Université Lille 1-Sciences et Technologies, 59655 Villeneuve d'Ascq, France

[‡]ARKEMA, Groupement de Recherches de Lacq, RD 817, B.P. 34, 64170 Lacq, France

Ⓢ *Supporting Information*

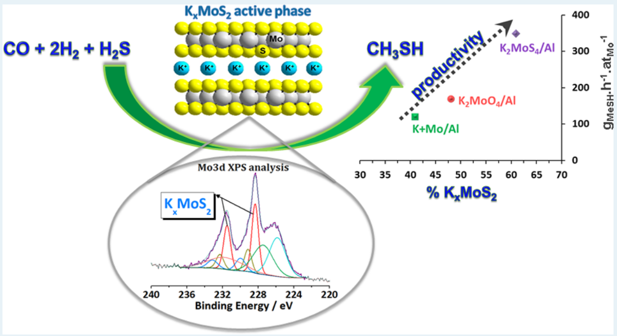

**ABSTRACT:** Alumina supported K-, Mo-, and K-Mo-based catalysts prepared from different precursors (ammonium heptamolybdate + $KNO_3$, $K_2MoO_4$, $K_2MoS_4$) with the same loading were used to produce $CH_3SH$ by the simple syngas/$H_2S$ route. The simultaneous presence of Mo and K in the catalytic system allows the achievement of higher CO conversions and $CH_3SH$ selectivity and a decrease in $CO_2$ selectivity. Through XPS analysis of sulfided catalysts, the presence of a new phase (named $K_xMoS_2$) with an unusual Mo 3d binding energy in which potassium cations are intercalated between the $MoS_2$ layers is evidenced. The amount of this phase was well correlated with the catalytic performances of the corresponding catalysts in the reaction of methyl mercaptan production. Indeed, it was found that the higher the amount of $K_xMoS_2$ phase in the catalyst, the higher the $CH_3SH$ productivity. On the basis of these statements $K_xMoS_2$ is proposed as the active phase acting in the reaction of thiolation of syngas.

**KEYWORDS:** *methyl mercaptan, thiolation, syngas, molybdenum disulfide, KMo-based catalysts, sulfided catalysts, potassium tetrathiomolybdate, potassium tetraoxomolybdate*

## 1. INTRODUCTION

Currently, methyl mercaptan ($CH_3SH$) is an industrially important chemical used as a raw material for the production of valuable organosulfur compounds such as methionine[1−3] (an important amino acid used as poultry feed supplement), dimethyl disulfide[4,5] (sulfiding agent for hydrotreating catalysts), and methanesulfonic acid[6,7] (acidic catalyst). Methyl mercaptan is currently manufactured on an industrial scale by the reaction of methanol with hydrogen sulfide.[8−11] Even if the production of methyl mercaptan via methanol/hydrogen sulfide is an efficient process that produces high methanol conversion and methyl mercaptan yields, this route needs a multiple-step pathway for the synthesis of methanol, which results in raised costs of production. This is the main reason why the development of a new route, which may provide greater economies by using a simple feedstock (syngas/hydrogen sulfide), is increasingly attractive in industrial applications. The production of methyl mercaptan from the one-step reaction of syngas and hydrogen sulfide has been studied since the 1980s. Its production on a laboratory scale is usually carried out using K−Mo-based catalysts with alumina[12−14] or silica as carrier.[15−20]

Yang et al.[15] studied the use of $K_2MoS_4/SiO_2$ and $MoS_2/K_2CO_3/SiO_2$ catalysts in the one-step synthesis from high-$H_2S$-content syngas and found that $K_2MoS_4/SiO_2$ was the more effective catalyst. The results of XRD suggested the presence of a named "Mo−S−K" phase that has been claimed to be responsible for the high activity and selectivity in $CH_3SH$ synthesis. Correlating these results with XPS analysis, the authors proposed that the presence of $(S{-}S)^{2-}$ on the catalyst surface inhibits the formation of the Mo−S−K phase, explaining the lower catalytic performance of $MoS_2/K_2CO_3/SiO_2$ in comparison to $K_2MoS_4/SiO_2$. The same team[16,21] studied the promoting effect of transition-metal oxides (Fe, Co, Ni) and rare-earth oxides (La, Ce) on $K_2MoS_4/SiO_2$ catalysts. It was found that the addition of promoters positively affects the catalytic performance of these catalysts. The results of XRD characterization showed that two main phases are present in promoted and unpromoted $K_2MoS_4/SiO_2$ catalysts: $Mo^{IV}S_2$ and $Mo^{VI}$−S−K. The addition of promoters is proposed to increase the concentration of Mo−S−K active sites because the decomposition of $K_2MoS_4$ to $MoS_2$ is restrained, suppressing deep reduction of $Mo^{VI}$ to $Mo^{IV}$.

**Received:** December 17, 2014
**Revised:** March 12, 2015
**Published:** March 31, 2015

ACS Publications

DOI: 10.1021/cs502031f
*ACS Catal.* 2015, 5, 2966−2981

The synthesis of methanethiol from $H_2S$-rich syngas over sulfided Mo based $SiO_2$ supported catalysts was also investigated by Chen et al.[18,19] Mo catalyst was modified by the addition of K and Co. It was observed that catalysts without alkali promoters ($Mo/SiO_2$ and $MoCo/SiO_2$) exhibit low CO conversion and low selectivity to $CH_3SH$, with COS being the main product. Meanwhile, the potassium-promoted Mo-based catalysts revealed the highest conversion of CO and the highest selectivity to $CH_3SH$, but selectivity toward $CO_2$ was also important. The work was focused on the pathway study showing that COS was formed from the reaction of $H_2S$ and CO primarily while hydrogenation and hydrolysis of COS leaded to $CH_3SH$ (and $H_2O$) and $CO_2$ and $H_2S$, respectively. The water-gas shift reaction was the main source of $CO_2$. The same authors indicated from XPS and ESR analysis that on Mo−(K)--(Co)/$SiO_2$ catalysts the reducibility of Mo species diminished in the presence of potassium, resulting in $Mo^{5+}$ species stabilized on the promoted catalysts after sulfidation, while $Mo^{4+}$ species are preferable on the potassium-free catalysts.[19]

Recently, Gutiérrez et al.[22] explored the catalytic properties of $K_2MoO_4/SiO_2$ sulfide supported catalysts in the synthesis of methanethiol from COS and $CS_2$. A study of the reaction mechanism showed that COS decomposes to CO and $H_2S$ and in parallel COS disproportionation leads to CO and $CS_2$, which is the reaction intermediate further hydrogenated to $CH_3SH$. According to these authors, catalyst characterization (XRD, Raman, and NO adsorption) suggests that two active phases are present on the sulfided catalyst, $MoS_2$ favoring the decomposition of COS to CO and a $K^+$-decorated $MoS_2$ promoting the disproportionation of COS and hydrogenation of the resulting $CS_2$. Addition of Co to the catalytic system[20] is shown to accelerate all of the previous individual reactions, COS disproportionation, hydrogenation, and hydrogenolysis ($CH_3SH$ to $CH_4$) by forming $K^+$- and Co-promoted $MoS_2$ slabs as usually admitted for the well-known CoMoS HDS catalyst active phase.[23] The same study leading to the same conclusions was extended to potassium-doped $MoS_2$ catalysts supported on alumina.[24] In a recent paper related to the synthesis of methanethiol from COS and $CS_2$, Gutierrez and co-workers detailed the mechanism of $CS_2$ hydrogenation using K-, Co-, and Ni-promoted $Mo/SiO_2$ catalysts.[25]

In an overview of earlier works concerning the synthesis of methyl mercaptan, most of the research has been focused on the development of efficient catalytic systems based principally on K−Mo supported catalysts and the determination of the reaction mechanisms starting from $CO/H_2/H_2S$ or $COS(CS_2)/H_2$ reactants. Concerning the active phase, its exact nature remains unclear. The aim of this work is to determine the active phase driving the catalytic performance in the methanethiol synthesis from $CO/H_2/H_2S$ using various alumina supported catalysts with the same Mo (8.1 wt %) and/or K (6.6 wt %) loadings starting from different precursors. Characterizations have been performed using Raman spectroscopy as well as TEM analysis. The most relevant data have been obtained from XPS analysis of catalysts before and after activation using careful decomposition of the Mo 3d spectra, allowing the proposal of correlations between catalytic performance and surface phase analysis.

## 2. EXPERIMENTAL SECTION

**2.1. Preparation of $K_2MoS_4$ Precursor.** Presulfided precursor, $K_2MoS_4$, was synthesized in the laboratory with a two-step procedure. The first step involved the preparation of ammonium tetrathiomolybdate ($(NH_4)_2MoS_4$, ATTM), according to a procedure described by Harmer and Sykes.[26] High-purity $H_2S$ was bubbled through a solution containing 50 g of ammonium heptamolybdate (HMA), $(NH_4)_6Mo_7O_{24}\cdot 4H_2O$ (Fluka, purity ≥99.0%), and 650 mL of ammonium hydroxide (Sigma-Aldrich, ∼25% $NH_3$ basis) for about 60 min. Since the reaction is exothermic, the synthesis was considered complete when the temperature began to drop. During that period, the solution became yellow and then dark red with formation of brown-red crystals ,which were filtered off, washed with ethanol (Sigma-Aldrich, purity ≥99.5%), and then dried under vacuum. The reaction yield was close to 97%. The second step consisted of the preparation of potassium tetrathiomolybdate ($K_2MoS_4$). In a typical preparation, 10 g of ATTM obtained in the first step was dissolved in 100 mL of a 2 M potassium hydroxide (Sigma-Aldrich, flakes, purity 90%) aqueous solution. The ammonia formed due to the basicity of the solution was evacuated by vacuum pumping. After complete removal of $NH_3$, a solution containing $K^+$ and $MoS_4^{2-}$ ions was obtained. $K_2MoS_4$ solid was precipitated in ethanol. A yield close to 98% was achieved. The presulfided salt was stored under vacuum.

**2.2. Catalyst Preparation.** Mo-, K-, and Mo−K-based catalysts were prepared by an incipient wetness impregnation method using $\gamma$-$Al_2O_3$ ("Al" noted) (pellets, SSA = 248 $m^2\ g^{-1}$, water pore volume $V_p$ = 1.11 $cm^3\ g^{-1}$) as support. For comparison purposes a Na-based catalyst was also prepared. For all of these solids, the Mo and K(Na) amounts were fixed to 8.1 and 6.6(3.9) wt %, respectively, corresponding to a K(Na)/Mo atomic ratio equal to 2. A series of six catalysts was thus prepared as follows.

(1) $K_2MoO_4$/Al and (2) $Na_2MoO_4$/Al solids were prepared by impregnation of solutions containing $K_2MoO_4$ (Aldrich, purity 98.0%) and $Na_2MoO_4$ (Sigma-Aldrich, purity ≥99.5%), respectively, on $Al_2O_3$. The resultant solids were maturated under a steamy atmosphere for 2 h and dried overnight at 80 °C.

(3) $K_2MoS_4$/Al catalyst was obtained by impregnation of a solution containing the prepared $K_2MoS_4$ precursor followed by maturation under a steamy atmosphere for 2 h and dried under vacuum for 20 h at room temperature.

(4) K+Mo/Al catalyst was prepared using a two-step impregnation procedure. In a first step, a solution containing Mo (0.17 g $mL^{-1}$ of ammonium heptamolybdate (AHM, Fluka, purity ≥99.0%) was pore volume impregnated on the support, followed by maturation (2 h under a steamy atmosphere), drying (overnight at 80 °C), and calcination (490 °C at 50 °C $h^{-1}$ for 2 h). Then, a solution containing K (0.19 g $mL^{-1}$ $KNO_3$, Fluka, purity ≥98.0%) was pore volume impregnated on the solid containing Mo. K+Mo/Al solid was obtained after maturation under a steamy atmosphere for 2 h, drying overnight at 80 °C, and calcination under air (490 °C at 50 °C $h^{-1}$ for 2 h).

For (5) K/Al and (6) Mo/Al catalysts, solutions containing $KNO_3$ (Fluka, purity ≥98.0%) or ammonium heptamolybdate (AHM; Fluka, purity ≥99.0%) with concentrations of 0.17 and 0.15 g $mL^{-1}$, respectively, were impregnated on the support, followed by maturation under a steamy atmosphere for 2 h. Then, the obtained solids were dried overnight at 80 °C and calcined under air (490 °C at 50 °C $h^{-1}$ for 2 h).

(7) Additionally, a highly loaded catalyst using $K_2MoO_4$ precursor was also prepared using the same procedure as for

catalysts (1). The amount of Mo of this solid was fixed at 17.9 wt %.

Table 1 summarizes for each catalyst the nomenclature used, the Mo and/or K content, and the precursors employed.

**Table 1. Nomenclature, Mo and K Loadings, and Precursors Used for All Catalysts**

| | amt, wt % | | | |
|---|---|---|---|---|
| catalyst | Mo | K(Na) | precursor | synthesis reference[a] |
| $K_2MoO_4$/Al | 8.1 | 6.6 | $K_2MoO_4$ | 1 |
| $Na_2MoO_4$/Al | 8.1 | 3.9 | $Na_2MoO_4$ | 2 |
| $K_2MoS_4$/Al | 8.1 | 6.6 | $K_2MoS_4$ | 3 |
| K+Mo/Al | 8.1 | 6.6 | $KNO_3$ and AHM | 4 |
| Mo/Al | 8.1 | | AHM | 5 |
| K/Al | | 6.6 | $KNO_3$ | 6 |
| $K_2MoO_4$/Al | 17.9 | 14.6 | $K_2MoO_4$ | 7 |

[a] These values correspond to the synthesis number referenced in the text, added for clarity.

Mo, K, and Na contents were verified by ICP analysis (Service Central d'Analyses CNRS), and ICP values did not show any deviation from the experimental values.

**2.3. Characterizations.** UV−visible spectroscopy was used to determine the purity of the thiomolybdate salt $K_2MoS_4$. Absorption spectra of the samples were recorded by using a PerkinElmer Lambda 650 UV−vis spectrophotometer. The spectrometer contains a double beam and a monochromator. The sources used were tungsten−halogen and deuterium. Spectra of liquid samples were recorded between 200 and 600 nm with a step of 1 nm. The molar extinction coefficient was calculated by using the Beer−Lambert law ($A = \varepsilon cl$, where $A$ is the absorbance, $\varepsilon$ is the molar extinction coefficient expressed in L mol$^{-1}$ cm$^{-1}$, $c$ is the concentration of the sample expressed in mol L$^{-1}$, and $l$ is the length of the cell expressed in cm).

The Raman spectra of the samples were recorded at room temperature using a Raman LabRam infinity microprobe (Jobin Yvon), equipped with a photodiode array detector in the spectral zone 100−1600 cm$^{-1}$. The exciting light source was the 532 nm line of an Nd:YAG laser, and the wavenumber accuracy was ±4 cm$^{-1}$. The Raman spectrometer was calibrated using the silicon line at 521.2 cm$^{-1}$.

The composition and chemical state of the elements were studied using X-ray photoelectron spectroscopy (XPS) on a KRATOS Axis Ultra spectrometer equipped with monochromatic Al K$\alpha$ (1486.6 eV) X-ray radiation (powered at 100 W). The analysis chamber was operated under ultrahigh vacuum with a pressure close to $10^{-10}$ Torr. The binding energy values were referred to the Al 2p peak at 74.6 eV. Simulation of the experimental photopeaks was carried out using a mixed Gaussian/Lorentzian peak fit procedure according to the software supplied by Casa XPS. Shirley background subtraction was used for atomic concentration calculation. The surface atomic concentrations were calculated by correcting the intensities with theoretical sensitivity factors based on Wagner cross sections.

The transmission electron microscopy (TEM) images were obtained using a TECNAI electron microscope operating at an accelerating voltage of 200 kV. For the preparation of the sample grid, the sample was ground into a fine powder and dispersed in ethanol. A very small drop of ethanol with suspended particles was dropped onto a holey-carbon copper grid. The grid was loaded into the sample chamber. The analysis was conducted under high vacuum.

**2.4. Catalyst Activation.** Prior to the catalytic test, the catalysts were in situ sulfided using a three-step procedure as follows:

first step: drying under $N_2$ flow (20 NL h$^{-1}$) from room temperature to 250 °C (2 °C/min)
second step: sulfidation under $H_2S$ flow (10 NL h$^{-1}$) at 250 °C for 1 h
third step: sulfidation with $H_2/H_2S$ flow (20 NL h$^{-1}$/5 NL h$^{-1}$) from 250 to 350 °C (2 °C/min) over 1 h at 350 °C

The same procedure was applied for the ex situ sulfidation of catalysts used for Raman, XPS, and HRTEM characterization. The samples sulfided for this purpose were carefully kept in a special cell under an atmosphere containing the sulfidation mixture. To avoid air exposure, Raman spectra were carried out through this special cell and XPS sampling was performed under an argon atmosphere in a glovebox connected to the XPS transfer chamber of the spectrometer.

For clarity purposes, the dried and/or calcined solids before activation will be called "catalysts", while the solids obtained after activation will be called "activated catalysts".

**2.5. Catalytic Activity Measurement.** $CH_3SH$ synthesis was carried out using a fixed-bed reactor placed in a temperature- controlled oven. The temperature was monitored and controlled at four points, feed line, product line, catalyst, and oven, using K-type thermocouples. External electric heaters with heating bands were used to keep the feed line and product line at about 120 °C. All of the heated parts were well insulated, to minimize energy losses and temperature gradients in the system. The feed gases (CO, $H_2$, $H_2S$, and $N_2$) were supplied from cylinders, and the flow rate of each gas was controlled individually by a mass flow controller. The operating conditions of the activity tests (flow, temperature, and pressure) were computer monitored. The outlet reactants (CO, $H_2S$, and $H_2$) and products ($CH_3SH$, COS, $CO_2$, $CS_2$, $CH_4$, and $CH_3SCH_3$) were analyzed by a gas chromatograph (GC; Agilent 6890N) equipped with an hp-plot Q column and a thermal conductivity detector (TCD). The performances were estimated for 30 mL of catalyst at three different temperatures, 280, 300, and 320 °C, using the following conditions: 10 bar of pressure, $H_2S/H_2/CO$ molar ratio equal to 1/2/1, gas hourly space velocity equal to 1333.33 h$^{-1}$ (total flow rate 40 NL h$^{-1}$). After the pretreatment stage (activation), the temperature was decreased until 280 °C, the initial temperature of the catalytic test. The reactants were introduced at the required $H_2S/H_2/CO$ ratio, and the pressure was increased at 10 bar. After about 15 h of stabilization (one night) the outlet gas mixture was analyzed by GC. The temperature was then increased to 300 °C. After stabilization, the products were analyzed. The same procedure was applied at 320 °C.

## 3. RESULTS AND DISCUSSION

The precursor potassium tetrathiomolybdate ($K_2MoS_4$) was characterized by Raman and UV−visible spectroscopy. These results are included in Figures S1 and S2 in the Supporting Information.

**3.1. Characterization of Catalysts.** Mo/Al, K/Al, and K+Mo/Al were characterized after calcination, whereas $K_2MoO_4$/Al, $Na_2MoO_4$/Al, and $K_2MoS_4$/Al were characterized after drying, in accord with their preparation procedure.

DOI: 10.1021/cs502031f
ACS Catal. 2015, 5, 2966−2981

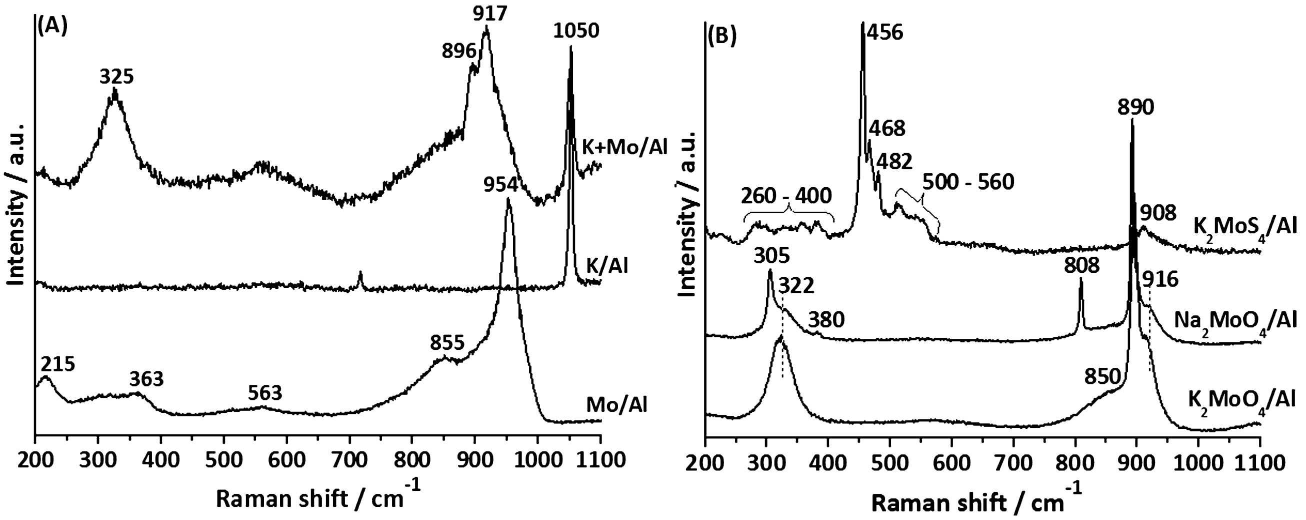

**Figure 1.** Raman spectra of (A) Mo/Al, K/Al, and K+Mo/Al catalysts and (B) $K_2MoO_4$/Al, $Na_2MoO_4$/Al, and $K_2MoS_4$/Al catalysts.

*3.1.1. Laser Raman Spectroscopy.* Figure 1A shows the Raman spectra of Mo/Al, K/Al, and K+Mo/Al catalysts. In the Raman spectrum of Mo/Al, five broad lines at 954, 855, 563, 363, and 215 $cm^{-1}$ were observed and attributed to the presence of well-dispersed $AlMo_6O_{24}H_6^{3-}$ Anderson heteropolyanion ($AlMo_6$) formed from alumina support dissolution upon its impregnation with a molybdenum-based aqueous solution, as reported by several authors.[27−29] The addition of potassium to the Mo-based catalyst results in a complete evolution of the K+Mo/Al Raman spectrum. For this solid, two main components were observed. The line at 1050 $cm^{-1}$ characterizes the $NO_3^-$ anion due to nitrate arising from the use of $KNO_3$ precursor,[30] as also observed for the solid K/Al. The very large line centered at 917 $cm^{-1}$ associated with the line at 325 $cm^{-1}$ shows the presence of dispersed monomolybdate $MoO_4^{2-}$ species absorbed on the support.[31,32] The presence of basic $MoO_4^{2-}$ entities indicates that the second-step impregnation with $KNO_3$ solution followed by a second calcination induces a decomposition of $AlMo_6$ heteropolyanion into monomolybdate entities at the alumina surface.

Figure 1B shows the Raman spectra of $K_2MoO_4$/Al and $Na_2MoO_4$/Al catalysts. The $K_2MoO_4$/Al spectrum displays a sharp line at 890 $cm^{-1}$ with a shoulder at 850 $cm^{-1}$ and a line at 322 $cm^{-1}$. These lines correspond to those of well-defined $K_2MoO_4$.[22,31,33,34] $Na_2MoO_4$/Al catalyst exhibits also narrow lines at 890, 808, 380, 322, and 305 $cm^{-1}$ attributed to the presence of bulk $Na_2MoO_4$.[32,35−37] In both Raman spectra, we can also observe a line at 916 $cm^{-1}$, which was attributed to adsorbed $MoO_4^{2-}$, as already observed for K+Mo/Al solid. However, this species, predominant in K+Mo/solid, is present to a lesser extent in $K_2MoO_4$/Al and $Na_2MoO_4$/Al. The narrow lines observed in these solids suggest that most of $K_2MoO_4$ and $Na_2MoO_4$ species were precipitated in the alumina porosity together with small quantities of adsorbed $MoO_4^{2-}$ species.

In Figure 1B the spectrum of $K_2MoS_4$/Al is also reported. It exhibits narrow lines at 482, 468, and 456 $cm^{-1}$ characteristic of bulk potassium tetrathiomolybdate,[37−39] indicating the preservation of $K_2MoS_4$ species after impregnation. Additionally, multiple small and wide Raman lines in the low-wavenumber region between 250 and 400 $cm^{-1}$ and others between 500 and 560 $cm^{-1}$ as well as the line at 908 $cm^{-1}$ were attributed to Mo−S or Mo−O bonds. These lines have not yet been clearly attributed to specific anions as $MoO_{4-x}S_x$ ($x$ = 1−3), but they indicate that a part of the $MoS_4^{2-}$ ions evolves with reoxidation during the impregnation of $K_2MoS_4$.

*3.1.2. X-ray Photoelectron Spectroscopy (XPS).* XPS analyses were carried out in order to obtain information about the oxidation state and dispersion of the different elements at the catalyst surface. The spectra of Mo/Al, K+Mo/Al, $K_2MoO_4$/Al, and $Na_2MoO_4$/Al catalysts in the Mo 3d region (Figure S3 in the Supporting Information) show the presence of two well-resolved spectral lines at 232.9 ± 0.2 and 236.0 ± 0.2 eV assigned to the Mo $3d_{5/2}$ and Mo $3d_{3/2}$ spin−orbit components, respectively. In this doublet, the positions are characteristics of $Mo^{VI}$ in an oxidic environment,[40,41] which is in agreement with the presence of $AlMo_6O_{24}H_6^{3-}$ species in the Mo-containing catalysts and $MoO_4^{2-}$ species in the K(Na)- and Mo-containing catalysts previously evidenced by Raman analysis.

$K_2MoS_4$/Al catalyst was also characterized by XPS analysis before activation. Figure 2 displays the XPS of the Mo 3d−S 2s region. The Mo 3d core level (with Mo $3d_{3/2}$ and Mo $3d_{5/2}$ spin−orbit components) of this solid is decomposed into three doublets: one doublet concerning sulfur species and two doublets concerning molybdenum species. The positions of the Mo $3d_{5/2}$ component of the two identified species were around 230.1 ± 0.2 and 232.2 ± 0.2 eV. The component located at the lowest binding energy (230.1 ± 0.2 eV) was assigned to a $Mo^{VI}$

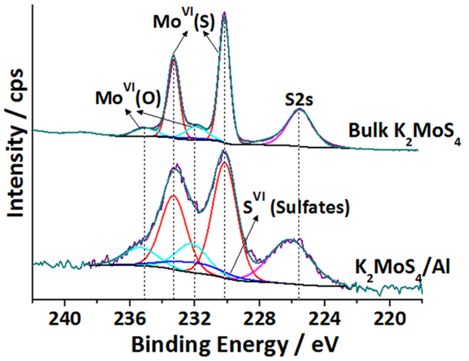

**Figure 2.** XPS spectra of the Mo 3d−S 2s core level of $K_2MoS_4$/Al catalyst and bulk $K_2MoS_4$.

species bonded to sulfur atoms, in agreement with the observation of this band at the same position as in the unsupported $K_2MoS_4$, as shown in Figure 2. The component positioned at 232.2 ± 0.2 eV corresponds to a $Mo^{VI}$ species in an oxidic environment.[40−42] This component was assigned to a reoxidized compound due to air exposure with Mo atoms bonded to oxygen atoms. Nevertheless, the predominant species (76%) is $Mo^{VI}(S)$, indicating that $K_2MoS_4$ is mainly maintained after deposition on alumina, as also deduced from Raman spectroscopy.

In order to investigate the dispersion of molybdenum on the alumina surface, the variation of the $(I_{Mo}/I_{Al})_{XPS}$ intensity ratio was plotted as a function of the bulk Mo/Al atomic ratio $(n_{Mo}/n_{Al})_{bulk}$ (Figure 3). These results were compared to the theoretical values calculated according to the monolayer model of Kerkhof and Moulijn (KM) and represented by the straight line plotted in Figure 3.[43] For Mo/Al and K+Mo/Al, almost no variation was observed between the experimental intensity ratios $I_{Mo}/I_{Al}$ measured and those calculated by the KM model, confirming that both samples adopt a monolayer dispersion with Mo species homogeneously distributed throughout the surface of the support. For $K_2MoO_4$/Al and $Na_2MoO_4$/Al catalysts a deviation from the KM model was observed. This result could be indicative of a multilayer deposition, assuming agglomeration of the impregnated species at the surface of support. This interpretation is supported by the narrow lines observed in the corresponding Raman spectra. A more important deviation from the KM model was observed for $K_2MoS_4$/Al catalyst, suggesting the presence of large particles of $K_2MoS_4$.

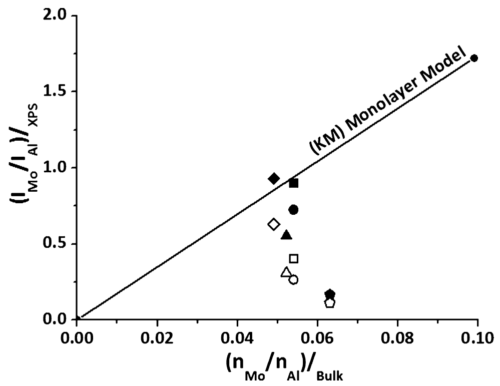

**Figure 3.** $(I_{Mo}/I_{Al})_{XPS}$ intensity ratio as a function of Mo/Al bulk atomic ratio of catalysts and activated catalysts: (◇) Mo/Al; (□) K+Mo/Al; (○) $K_2MoO_4$/Al; (△) $Na_2MoO_4$/Al; (⬠) $K_2MoS_4$/Al. The solid line corresponds to theoretical values calculated according to the KM model. Filled symbols are representative of catalysts, and open symbols are representative of activated catalysts.

On the basis of these statements, the fraction of Mo atoms detected by XPS $(Mo\%_{detXPS})$ was also calculated for these solids and is displayed in Table 2. $Mo\%_{detXPS}$ was calculated using the following formula: $Mo\%_{detXPS} = [(\text{Mo atom }\%)_{XPS})/(\text{Mo atom }\%)_{bulk}] \times 100$, where $(\text{Mo atom }\%)_{XPS}$ is the Mo atomic percentage obtained upon XPS analysis and $(\text{Mo atom }\%)_{bulk}$ is the global Mo bulk atomic percentage. Calculated values are shown in Table 2.

**Table 2. Mo % Detected by XPS before and after Activation**

| solid | $Mo\%_{detXPS}$ catalyst | $Mo\%_{detXPS}$ activated catalyst |
|---|---|---|
| Mo/Al | 97 | 71 |
| K+Mo/Al | 90 | 38 |
| $K_2MoO_4$/Al | 71 | 29 |
| $Na_2MoO_4$/Al | 59 | 32 |
| $K_2MoS_4$/Al | 25 | 16 |

As expected, in agreement with the good dispersion of Mo entities at the catalyst surface, an almost complete detection of Mo atoms was observed for Mo/Al and K+Mo/Al (97 and 90%, respectively). In contrast, for $K_2MoO_4$/Al and $Na_2MoO_4$/Al, the $Mo\%_{detXPS}$ was significantly lower (71 and 59 Mo%, respectively) as a result of the poor dispersion of Mo species in these solids. It is interesting to note that, if Mo and K are impregnated over alumina separately, a good dispersion is achieved, while when these species are impregnated from the same precursor, the agglomeration of supported species is observed. For $K_2MoS_4$/Al, only 25% of Mo is detected by XPS, confirming that $K_2MoS_4$/Al is the most poorly dispersed catalyst.

The low dispersion correlated to the formation of large particles blocking the pores is in agreement with the large decrease in $K_2MoO_4/Al_2O_3$ and $K_2MoS_4/Al_2O_3$ catalyst specific areas (168 and 144 $m^2\ g^{-1}$, respectively) in comparison to the initial alumina specific area value (280 $m^2\ g^{-1}$)

### 3.2. Catalytic Performance.

The overall reaction by which carbon monoxide (CO), hydrogen ($H_2$), and hydrogen sulfide ($H_2S$) are converted to methanethiol ($CH_3SH$) is[17,44−48]

$$CO + 2H_2 + H_2S = CH_3SH + H_2O \tag{1}$$

Reaction 1 is very exothermic ($\Delta_r H° = -132.9$ kJ $mol^{-1}$) and has no thermodynamic limitation.[49] It is believed that this reaction proceeds via hydrogenation of the intermediate carbonyl sulfide (COS) (reaction 3), which is formed upon the reaction of CO and $H_2S$ (reaction 2), according to

$$CO + H_2S = COS + H_2 \tag{2}$$

$$COS + 3H_2 = CH_3SH + H_2O \tag{3}$$

The experimental results of Barrault et al.[48] showed that reaction 2 is very fast in comparison to reaction 3, the latter being the rate-determining step for $CH_3SH$ formation.

Moreover, $CO_2$ can be produced by disproportionation or hydrolysis of COS or by the water-gas shift reaction (reactions 4−6, respectively):[12,18,48]

$$2COS = CO_2 + CS_2 \tag{4}$$

$$COS + H_2O = CO_2 + H_2S \tag{5}$$

$$CO + H_2O = CO_2 + H_2 \tag{6}$$

Finally, other reactions in which $CH_3SH$ is consumed may occur:[12,18]

$$CH_3SH + H_2 = CH_4 + H_2S \tag{7}$$

$$2CH_3SH = CH_3SCH_3 + H_2S \tag{8}$$

We must also mention that another mechanism was proposed by Gutiérrez et al. for the formation of $CH_3SH$.[22] These authors studied the reaction mechanism of the methylmercaptan synthesis using COS and $H_2$ as starting materials. They found in these conditions that the methyl mercaptan was formed via two steps: disproportionation of COS into $CO_2$ and $CS_2$ followed by $CS_2$ hydrogenation according to

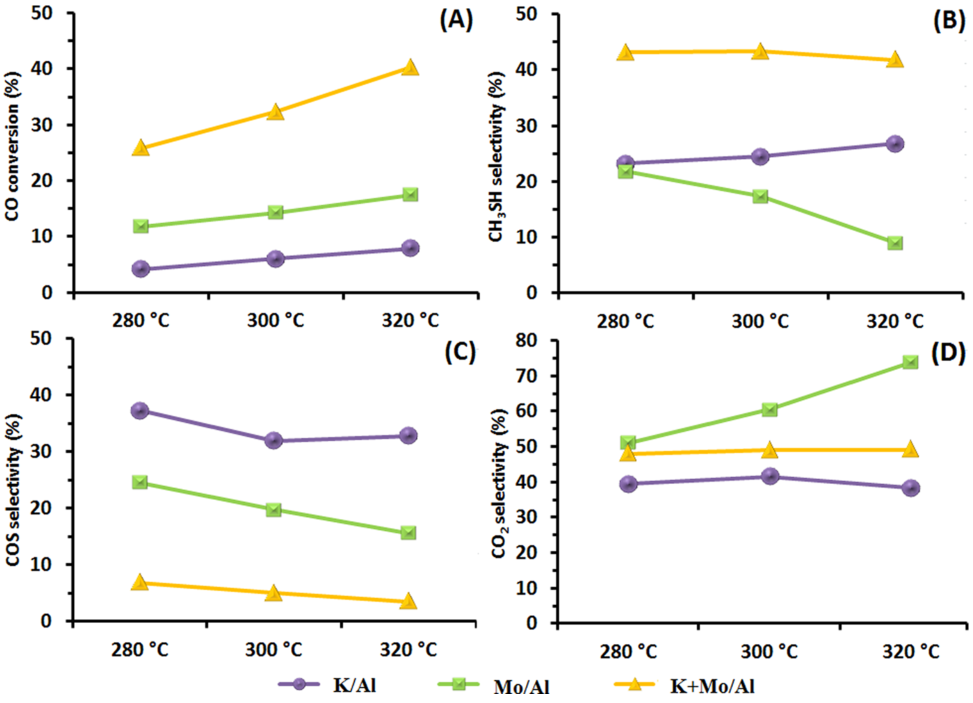

**Figure 4.** Evolution of the CO conversion (A) and selectivity in $CH_3SH$ (B), COS (C), and $CO_2$ (D) of K/Al, Mo/Al, and K+Mo/Al catalysts. Reaction conditions: 10 bar, 1333 $h^{-1}$, $CO/H_2/H_2S = 1/2/1$.

$$2COS = CO_2 + CS_2 \tag{4}$$

$$CS_2 + 3H_2 = CH_3SH + H_2S \tag{9}$$

The goal of this part is not to discuss the reaction mechanism but to point out the global effect of the different active elements (Mo and K), depending on the preparation methodologies that were used to obtain the corresponding catalysts.

*3.2.1. Effect of the Incorporation of Potassium.* The CO conversions and selectivities toward $CH_3SH$, COS, and $CO_2$ of activated catalysts K/Al, Mo/Al, and K+Mo/Al as a function of the reaction temperature are exposed in Figure 4.

Several points can be discussed.

(i) For these catalysts, the major products of reaction were methyl mercaptan ($CH_3SH$), carbonyl sulfide (COS), and carbon dioxide ($CO_2$). However, for some of the catalysts, a small quantity of other products was observed with selectivities of about 2% of $CS_2$ (reaction 4) for K/Al, about 2% of $CH_3SCH_3$ (reaction 8) for Mo/Al, and about 5% of $CH_4$ (reaction 7) for K+Mo/Al.

(ii) For these three solids, the conversion of CO increases linearly with temperature. The least active catalyst was K/Al, exhibiting a CO conversion between 4% and 8% over the range of temperatures evaluated. The CO conversion of Mo/Al was almost twice that of the former solid, and K+Mo/Al was 5 times more active than the solid without Mo and at least 2 times more active than the solid without K. This observation is the first evidence of the advantage of having both elements (K and Mo) in the catalytic system, revealing the synergetic effect between K and Mo for CO conversion.

(iii) In comparison to the Mo/Al and K/Al catalyst behavior, the high CO conversion obtained for K+Mo/Al catalyst is also related to high $CH_3SH$ selectivity (around 43%), confirming the beneficial use of both K and Mo elements for catalyst formulation, as already reported by several authors.[16,18,19] The high selectivity was almost constant over the temperature range studied. A constant selectivity in $CH_3SH$ was also observed for K/Al catalyst, but to a lesser extent (23%). For Mo/Al catalyst the $CH_3SH$ selectivity decreases with temperature until 8% at 320 °C and the $CH_3SH$ selectivity evolution is clearly the opposite of the $CO_2$ selectivity evolution.

(iv) Concerning the effect of each metal on the selectivities and conversions, especially at 300 and 320 °C, the following observations can be made. K/Al catalyst exhibits a low CO conversion and also a low COS conversion into $CH_3SH$ and $CO_2$ (COS acting as reaction intermediate, a high COS selectivity corresponds to a low COS conversion). Mo/Al catalyst displays a higher CO conversion and a higher COS conversion in comparison with K/Al; however, most of the COS was converted to $CO_2$ (whose selectivity at 320 °C is about 80%) instead of $CH_3SH$.

K+Mo/Al catalyst showed the highest CO and COS conversions among the three catalysts. For this solid, most of the COS is hydrogenated to $CH_3SH$ (reaction 2), as observed in Figure 4. Nevertheless, $CO_2$ is also observed but to a lesser extent (about 40−50%) than in Mo/Al, highlighting the fact that the presence of potassium inhibits $CO_2$ formation.

One possibility to explain this point is that the presence of K in the catalytic formulation inhibits the hydrolysis of COS into $CO_2$. This hypothesis has to be confirmed by future works. The simultaneous presence of K and Mo is thus probably beneficial for COS hydrogenation to form $CH_3SH$. The resulting $CH_3SH$ productivities are 15, 11, and 121 $g_{CH_3SH}\ h^{-1}\ L_{cat}^{-1}$ by using K/Al, Mo/Al, and K+Mo/Al catalysts, respectively (see Table 3).

*3.2.2. Comparison between K+Mo/Al and $K_2MoO_4$/Al Catalysts.* K+Mo/Al and $K_2MoO_4$/Al catalytic performances have been compared. The CO conversion and $CH_3SH$, COS, and $CO_2$ selectivities of both catalysts as a function of reaction temperature are shown in Figure 5. No significant differences between these two solids concerning the CO conversion and selectivities toward the main products $CH_3SH$, COS, and $CO_2$

Table 3. $CH_3SH$ Productivities of Activated Catalysts

| catalyst | $CH_3SH$ productivity ($g_{CH_3SH}$ $h^{-1}$ $L_{cat}^{-1}$) 280 °C | 300 °C | 320 °C |
|---|---|---|---|
| Mo/Al | 19 | 18 | 11 |
| K/Al | 7 | 11 | 15 |
| K+Mo/Al | 80 | 100 | 121 |
| $K_2MoO_4$/Al | 87 | 112 | 126 |
| $Na_2MoO_4$/Al | 82 | 106 | 108 |
| $K_2MoS_4$/Al | 90 | 122 | 141 |

are observed. As a result, the productivity of $CH_3SH$ reached by K+Mo/Al and $K_2MoO_4$/Al solids was very close, 121 and 126 g $h^{-1}$ $L_{cat}^{-1}$, respectively, as reported in Table 3. Nevertheless, $K_2MoO_4$/Al catalyst was obtained after drying without further calcination, while K+Mo/Al was obtained after two calcination steps. With regard to $CH_3SH$ productivity, it means that the incorporation of K and Mo coming from the same precursor is advantageous in terms of time and cost of preparation of catalysts, which are reduced when synthesizing $K_2MoO_4$/Al.

*3.2.3. Effect of the Alkali Promoter (K or Na) and Molybdenum Precursor.* $K_2MoO_4$/Al, $Na_2MoO_4$/Al, and $K_2MoS_4$/Al catalytic performances are assessed in this section and are displayed in Figure 6. $K_2MoO_4$/Al and $Na_2MoO_4$/Al were compared in order to study the effect of a different alkali promoter, and $K_2MoO_4$/Al and $K_2MoS_4$/Al were compared with the aim to investigate the influence of the initial precursor, either oxidic ($K_2MoO_4$) or sulfided ($K_2MoS_4$). On comparison of $K_2MoO_4$/Al and $Na_2MoO_4$/Al catalysts, no difference in CO conversion or in COS selectivity was observed. Nevertheless, a different trend in $CH_3SH$ and $CO_2$ selectivities was shown. A decrease in $CH_3SH$ selectivity (5%) and an increase in $CO_2$ selectivity (11%) is obtained with the catalyst promoted with Na, particularly at high temperature (320 °C). These results could suggest that, when K is replaced by Na, the hydrolysis of COS would be favored over the hydrogenation of COS to $CH_3SH$. Additionally, for $Na_2MoO_4$/Al no $CH_4$ production was observed but small amounts of $CS_2$ and $CH_3SCH_3$ (0.2% and 1.0%, respectively, at 320 °C) were detected. The absence of $CH_4$ and the decrease in $CH_3SH$ selectivity seem to indicate a lower hydrogenating effect of Na in comparison to K-based Mo catalysts.

On comparison of $K_2MoO_4$/Al and $K_2MoS_4$/Al, very little difference was observed between these two solids, meaning that the use of different precursors for introducing K and Mo in the same salt does not have a significant effect on the catalytic performances. The $CH_3SH$ productivity at 320 °C when using the catalyst $K_2MoS_4$/Al reaches 141 g $h^{-1}$ $L_{cat}^{-1}$ (Table 3).

**3.3. Activated Catalysts: Comprehension and Approach to the Active Phase.** Before testing, catalysts were activated in situ. The same procedure was applied for the ex situ sulfidation of catalysts used for X-ray photoelectron spectroscopy (XPS), Raman, and HRTEM characterization.

*3.3.1. XPS: Evidence of the New K(Na)−$Mo^{IV}$(S) Phase.* The surface composition and oxidation state of activated catalysts were analyzed by XPS. Figure 7 shows the spectra of the Mo 3d−S 2s region of activated Mo/Al, K+Mo/Al, $K_2MoO_4$/Al, $Na_2MoO_4$/Al, and $K_2MoS_4$/Al catalysts.

As can be seen, the global shape of the XPS spectrum of Mo/Al activated catalyst is similar to that of a classical HDS catalyst with two main peaks with an apparent maximum at about 229 eV attributed to $MoS_2$ nanocrystallites.[50,51] For solids containing K or Na, the shape of the XPS spectra is very different, with a particular broadening of these two main peaks and a shift of the maximum toward lower binding energies (about 228 eV), which means that at least one new contribution is observed. Changes are also observed regarding the S 2p spectra.

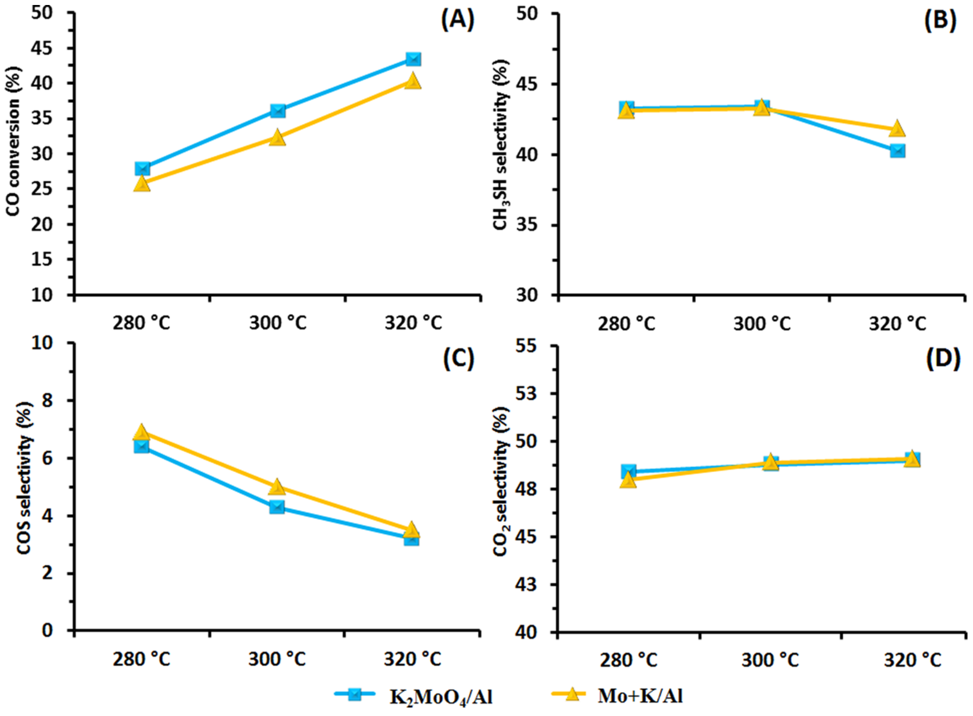

Figure 5. Evolution of the CO conversion (A) and selectivity in $CH_3SH$ (B), COS (C), and $CO_2$ (D) of K+Mo/Al and $K_2MoO_4$/Al catalysts. Reaction conditions: 10 bar, 1333 $h^{-1}$, $CO/H_2/H_2S$ = 1/2/1.

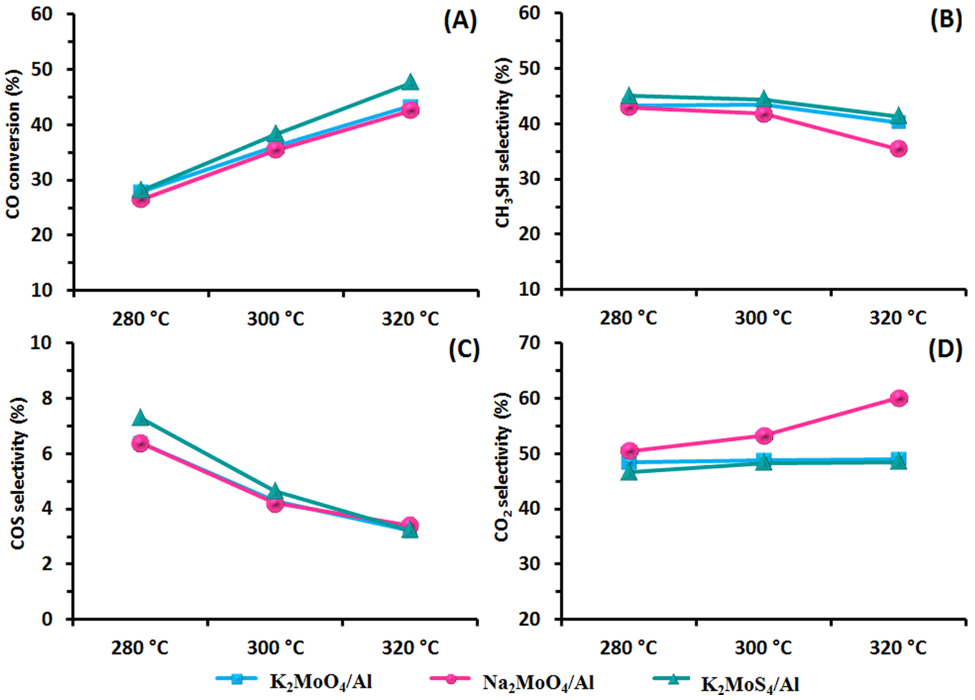

**Figure 6.** Evolution of the CO conversion (A) and selectivity in $CH_3SH$ (B), COS (C), and $CO_2$ (D) of $K_2MoO_4/Al$, $Na_2MoO_4/Al$, and $K_2MoS_4/Al$ catalysts. Reaction conditions: 10 bar, 1333 $h^{-1}$, $CO/H_2/H_2S$ = 1/2/1.

In Figure 8, upon introduction of K in the catalytic formulation, it is easily observed that the S 2p width is largely increased; this point will be discussed hereafter in section 3.3.2. We also note for K-containing activated catalysts a sulfur contribution due to sulfate type species at higher binding energy. Contact with air (oxygen) was clearly avoided after activation during the transfer in the XPS chamber, preventing oxygen contamination; sulfate species are formed in this case during the activation procedure. The presence of sulfate species is also reported in the literature for K-containing catalysts.[22] To interpret more deeply all of these observations, all of the XPS spectra were carefully decomposed.

In activated molybdenum catalysts, Mo and S coexist. The spectral envelope of Mo 3d covers the energy range of 227–238 eV as the chemical oxidation states of Mo vary from 0 to +VI, while that of S 2s covers the 224–235 eV range, which corresponds to S chemical states varying from -II to +VI, leading to the overlapping of both Mo 3d and S 2s BE regions. Therefore, the contribution of S 2s must be initially ruled out to obtain the true contribution of the Mo 3d level. The binding energies (BE), full widths at half-maximum (fwhms), and peak areas of S 2s contributions were directly deduced from those of the corresponding S 2p peaks using the constraints reported in Tables 4–6. Each S 2p contribution was thus simulated with two interdependent peaks corresponding to S $2p_{1/2}$ and S $2p_{3/2}$ core levels, taking into account the constraints in area, fwhm, and position as reported in Tables 4–6. Each Mo contribution was simulated with a doublet corresponding to Mo $3d_{3/2}$ and Mo $3d_{5/2}$ core levels. As the spectral characteristics of Mo $3d_{3/2}$ and Mo $3d_{5/2}$ peaks were interdependent, each doublet was simulated using constraints in area, fwhm, and BE as also reported in Tables 4–6.

(i) *A–C* and *J–L* are the values of areas of main XPS peaks that were calculated by the CASA software to give a good fit between the experimental XPS spectra and the corresponding simulated spectra while respecting all the constraints which were imposed between these peaks and all other peaks (these constraints being deduced from theoretical considerations and adjusted from experimental data).

(ii) *D–F* and *M–O* are the values of the fwhms of main XPS peaks that were calculated by the CASA software to give a good fit between the experimental XPS spectra and the corresponding simulated spectra while respecting all the constraints which were imposed between these peaks and all other peaks (these constraints being deduced from experimental data).

(iii) *G–I* and *P–R* are the values of the positions (binding energies, BE) of main XPS peaks that were calculated by the CASA software to give a good fit between the experimental XPS spectra and the corresponding simulated spectra, while respecting all the constraints that were imposed between these peaks and other peaks (these constraints being deduced from experimental data).

For the five Mo-based catalysts (Figure 7), three different distributions of Mo species were identified. The first one is obtained for Mo/Al, the second one for K+Mo/Al, and the last one for $K_2MoO_4/Al$, $Na_2MoO_4/Al$, and $K_2MoS_4/Al$ activated catalysts.

(1) The constraints (Mo 3d and S 2p) used for the decomposition of activated Mo/Al catalyst spectrum are presented in Table 4. The exact positions of the Mo $3d_{5/2}$ peaks of each doublet and their corresponding assignment are gathered in Table 7. The Mo 3d spectrum is decomposed into three doublets regarding Mo (three Mo species) and two S 2s doublets (two sulfur species). This solid exhibits, as usually reported for classical CoMo hydrotreatment catalysts, the three well-known Mo doublets whose Mo $3d_{5/2}$ components are placed at 228.9, 230.4, and 232.6 eV according to three oxidation states of molybdenum, $Mo^{IV}$, $Mo^{V}$, and $Mo^{VI}$, respectively.[50−52] The first contribution is attributed to the $MoS_2$ phase, the second contribution is attributed to $Mo^V$ surrounded by oxygen and sulfur atoms (intermediate sulfidation phase, denoted $Mo^V$–OS), and the contribution at

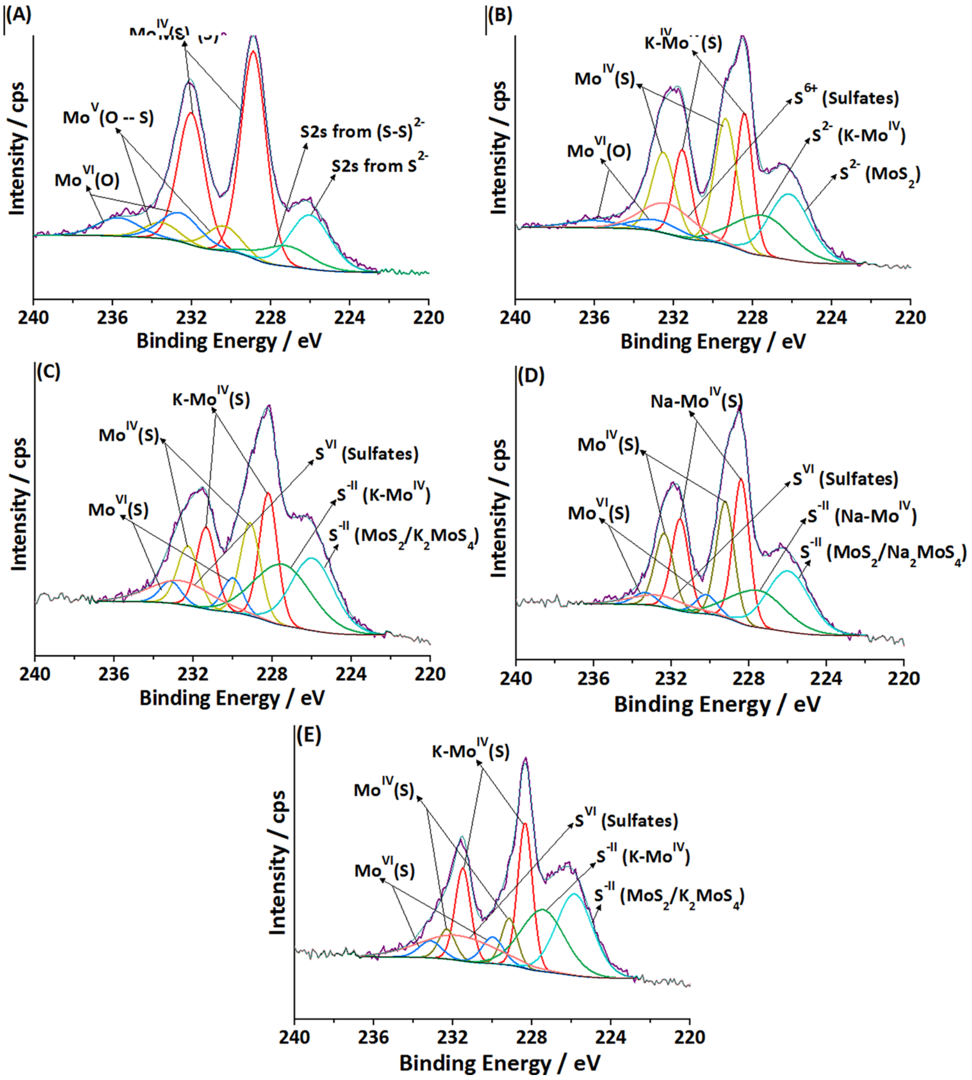

**Figure 7.** XPS spectra of the Mo 3d–S 2s core level of activated catalysts: (A) Mo/Al; (B) K+Mo/Al; (C) $K_2MoO_4$/Al; (D) $Na_2MoO_4$/Al; (E) $K_2MoS_4$/Al.

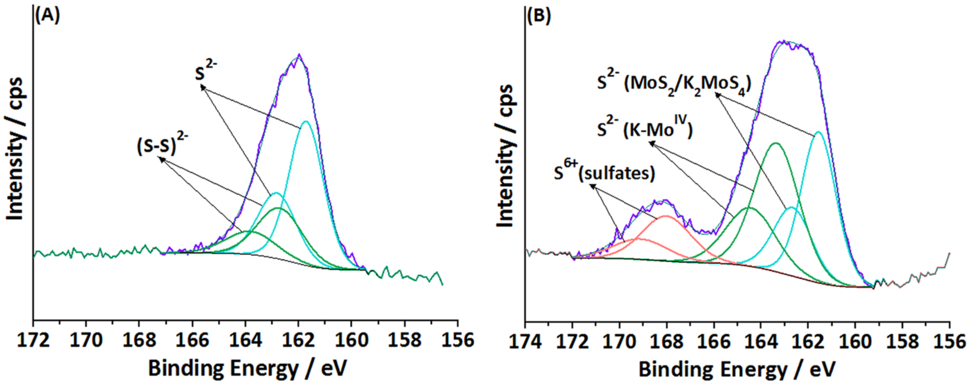

**Figure 8.** XPS spectra of the S 2p core level of activated catalysts (A) Mo/Al and (B) $K_2MoO_4$/Al.

higher binding energy is assigned to oxidized $Mo^{VI}$ species (denoted $Mo^{VI}$–O).

(2) The Mo 3d photopeak of K+Mo/Al activated catalyst cannot be decomposed in a satisfactory way with the same three components previously used for Mo/Al catalyst. A careful decomposition (see Table 5) taking into account the whole Mo 3d envelope led to three Mo doublets whose Mo $3d_{5/2}$ components are located at 228.4, 229.4, and 232.9 eV (see Table 7). The components at 229.4 and 232.9 eV are attributed to $Mo^{IV}$ species ($MoS_2$) and $Mo^{VI}$ in oxidic environments, respectively, found as well in the Mo/Al activated catalyst. The third doublet is an unusual contribution at 228.4 eV shifted toward lower binding energy (1.0 eV) in comparison to the Mo binding energy (229.4 eV) ascribed to the $MoS_2$ phase. The

### Table 4. XPS Parameters Used for the Decomposition of Mo 3d and S 2p Spectra of Activated Mo/Al

| species | peak | constraint area | constraint fwhm | constraint BE (eV) |
|---|---|---|---|---|
| $S^{2-}$ ($MoS_2$) | S $2p_{3/2}$ | $A$ | $D$ = $\text{fwhm}_{\text{Al 2p}} \times \alpha$[a] | $G$ = 162.1; 161.1[b] |
| | S $2p_{1/2}$ | $A \times 0.5$ | $D \times 1.1$ | $G + 1.1$ |
| $S_2^{2-}$ ($Mo^V$−OS) | S $2p_{3/2}$ | $B$ | $E = D \times 1.3$ | $H$ = 163.4; 162.4 |
| | S $2p_{1/2}$ | $B \times 0.5$ | $E \times 1.1$ | $H + 1.1$ |
| $S^{2-}$ ($MoS_2$) | S 2s | $(1.5 \times A)/1.7$; $(1.5 \times A)/1.4$ | $D \times 1.5$ | $(G + 65)$; $(G + 64)$ |
| $S_2^{2-}$ ($Mo^V$−OS) | S 2s | $(1.5 \times B)/1.7$; $(1.5 \times B)/1.4$ | $E \times 1.5$ | $(H + 65)$; $(H + 64)$ |
| $Mo^{IV}$ ($MoS_2$) | Mo $3d_{5/2}$ | $J$ | $M$ = $\text{fwhm}_{\text{Al 2p}} \times \beta$[a] | $P$ = 229.5; 228.8 |
| | Mo $3d_{3/2}$ | $J \times 0.67$ | $M \times 1.05$ | $P + 3.15$ |
| $Mo^V$ ($Mo^V$−OS) | Mo $3d_{5/2}$ | $K$ | $N$ = $\text{fwhm}_{\text{Al 2p}} \times \gamma$[a] | $Q$ = 231.3; 230.3 |
| | Mo $3d_{3/2}$ | $K \times 0.67$ | $N \times 1.05$ | $Q + 3.15$ |
| $Mo^{VI}$ ($Mo^{VI}$−O) | Mo $3d_{5/2}$ | $L$ | $O$ = $\text{fwhm}_{\text{Al 2p}} \times \delta$[a] | $R$ = 233.2; 232.5 |
| | Mo $3d_{3/2}$ | $L \times 0.67$ | $O \times 1.05$ | $R + 3.15$ |

[a] The fwhm constraints ($D$ and $M$−$O$) regarding S $2p_{3/2}$ and Mo $3d_{5/2}$ are obtained from experimental data using the fwhm of Al 2p. $\alpha = 0.9 \pm 0.1$; $\beta = 0.8 \pm 0.2$; $\gamma = 1.0 \pm 0.1$; $\delta = 1.5 \pm 0.3$. [b] E.g. "$G$ = 162.1; 161.1" means that the value of the BE can evolve during the fit between 161.1 and 162.1 eV.

### Table 5. XPS Parameters Used for the Decomposition of Mo 3d and S 2p Spectra of Activated K+Mo/Al

| species | peak | constraint area | constraint fwhm | constraint BE (eV) |
|---|---|---|---|---|
| $S^{2-}$ ($MoS_2$) | S $2p_{3/2}$ | $A$ | $D$ = $\text{fwhm}_{\text{Al 2p}} \times \alpha$[a] | $G$ = 162.1; 161.1[b] |
| | S $2p_{1/2}$ | $A \times 0.5$ | $D \times 1.1$ | G + 1.1 |
| $S^{2-}$ (K−$Mo^{IV}$(S)) | S $2p_{3/2}$ | $B$ | $E = D \times 1.3$ | $H$ = 163.4; 162.4 |
| | S $2p_{1/2}$ | $B \times 0.5$ | $E \times 1.1$ | $H + 1.1$ |
| $SO_4^{2-}$ | S $2p_{3/2}$ | $C$ | $F$ | $I$ = 168.3; 167.3 |
| | S $2p_{1/2}$ | $C \times 0.5$ | $F \times 1.1$ | $I + 1.1$ |
| $S^{2-}$ ($MoS_2$) | S 2s | $(1.5 \times A)/1.7$; $(1.5 \times A)/1.4$ | $D \times 1.5$ | $(G + 65)$; $(G + 64)$ |
| $S^{2-}$ (K−$Mo^{IV}$(S)) | S 2s | $(1.5 \times B)/1.7$; $(1.5 \times B)/1.4$ | $E \times 1.5$ | $(H + 65)$; $(H + 64)$ |
| $SO_4^{2-}$ | S 2s | $(1.5 \times \text{C})/1.7$; $(1.5 \times C)/1.4$ | $F \times 1.5$ | $(I + 65)$; $(I + 64)$ |
| $Mo^{IV}$ ($MoS_2$) | Mo $3d_{5/2}$ | $J$ | $M$ = $\text{fwhm}_{\text{Al 2p}} \times \beta$[a] | $P$ = 229.5; 228.8 |
| | Mo $3d_{3/2}$ | $J \times 0.67$ | $M \times 1.05$ | $P + 3.15$ |
| $Mo^{IV}$ (K−$Mo^{IV}$(S)) | Mo $3d_{5/2}$ | $K$ | $N$ = $\text{fwhm}_{\text{Al 2p}} \times \varepsilon$[a] | $Q$ = 228.6; 227.8 |
| | Mo $3d_{3/2}$ | $K \times 0.67$ | N × 1.05 | $Q + 3.15$ |
| $Mo^{VI}$ ($Mo^{VI}$−O) | Mo $3d_{5/2}$ | $L$ | $O$ = $\text{fwhm}_{\text{Al 2p}} \times \delta$[a] | $R$ = 233.2; 232.5 |
| | Mo $3d_{3/2}$ | $L \times 0.67$ | $O \times 1.05$ | $R + 3.15$ |

[a] The fwhm constraints ($D$ and $M$−$O$) regarding S 2p3/2 and Mo 3d5/2 are obtained from experimental data using the fwhm of Al 2p. $\alpha = 0.9 \pm 0.1$; $\beta = 0.8 \pm 0.2$; $\varepsilon = 0.6 \pm 0.2$; $\delta = 1.5 \pm 0.3$. [b] E.g. "$G$ = 162.1; 161.1" means that the value of the BE can evolve during the fit between 161.1 and 162.1 eV.

binding energy at 228.4 eV is too low to be related to $Mo^V$—as already identified in Mo/Al—whose binding energy is expected between that of $Mo^{IV}$ in $MoS_2$ and that of $Mo^{VI}$ (oxide).

(3) The constraints used for the decomposition of activated $K_2MoO_4$/Al, $Na_2MoO_4$/Al, and $K_2MoS_4$/Al are presented in Table 6. Three Mo doublets must be used to decompose the Mo 3d spectra of $K_2MoO_4$/Al, $Na_2MoO_4$/Al, and $K_2MoS_4$/Al activated catalysts with similar Mo $3d_{5/2}$ BEs of around 228.3(±0.1), 229.1(±0.1), and 230.1(±0.1) eV (see Table 7). The first component at 229.1 eV is attributed to the $MoS_2$ phase (also identified in Mo/Al and in K+Mo/Al). For these three sulfide catalysts, no $Mo^{VI}$ oxide phase contribution (between 230 and 231 eV) can be introduced in the decomposition, in accordance with the shape of the spectra. The second doublet at 230.0 eV is similar to that ascribed to $Mo^{VI}$ species in sulfur surroundings ($MoS_4$-type entities) observed in the Mo 3d spectra of bulk $K_2MoS_4$ and $K_2MoS_4$/Al catalyst (Figure 4). It means that these $MoS_4$-type entities are still present after sulfidation in the case of $K_2MoS_4$/Al and are formed during the sulfidation procedure in the case of $K_2(Na_2)MoO_4$/Al. The component at the lowest binding energy (228.3 eV) is similar to that observed at 228.4 eV for K+Mo/Al activated solid and is thus probably due to the presence of the same entity. It is an unusual component never observed in a sulfided Co(Ni)Mo based hydrotreatment catalysts, and it is then assumed to be related to the presence of the high quantity of potassium (sodium) (K(Na)/Mo = 2) interacting with the $MoS_2$ phase. This new phase is denoted $K_xMoS_2$.

3.3.2. *Nature of the K−$Mo^{IV}$(S) Phase.* Literature data indicate unambiguously the efficiency of K−Mo supported catalysts for $CH_3SH$ from the $CO/H_2/H_2S$ mixture, but studies have been more focused on the reaction mechanisms than on active phase determination. From XRD measurements a $Mo^{6+}$−$S_x$−$K^+$ phase was first proposed as an active phase by Yang et al.[15,21] and Dai et al.[16] The main conclusion proposed by Chen et al.[19] from XPS analysis was that the addition of potassium increases the $Mo^V/Mo^{IV}$ and $(S^- + S^{2-})/SO_4^{2-}$ ratios, favoring the synthesis of $CH_3SH$. Gutiérrez et al.,[20] when working with a sulfided $K_2MoO_4/SiO_2$ catalyst for the reaction of disproportionation of COS, assumed that a fraction of $K^+$ adsorbs on $MoS_2$, resulting in the formation of a $K^+$-decorated $MoS_2$ phase where K cations would be distributed randomly on the $MoS_2$ surface, without modifying the crystalline structure of the $MoS_2$ cluster,

Table 6. XPS Parameters Used for the Decomposition of Mo 3d and S 2p Spectra of Activated $K_2MoO_4$/Al, $Na_2MoO_4$/Al, and $K_2MoS_4$/Al

| species[c] | peak | constraint area | constraint fwhm | constraint BE (eV) |
|---|---|---|---|---|
| $S^{2-}$ ($MoS_2$/$K_2MoS_4$)[d] | S $2p_{3/2}$ | $A$ | $D = \text{fwhm}_{\text{Al 2p}} \times \alpha$[a] | $G$ = 162.1; 161.1[b] |
| | S $2p_{1/2}$ | $A \times 0.5$ | $D \times 1.1$ | $G + 1.1$ |
| $S^{2-}$(K–$Mo^{IV}$(S)) | S $2p_{3/2}$ | $B$ | $E = D \times 1.3$ | $H$ = 163.4; 162.4 |
| | S $2p_{1/2}$ | $B \times 0.5$ | $E \times 1.1$ | $H + 1.1$ |
| $SO_4^{2-}$ | S $2p_{3/2}$ | $C$ | $F$ | $I$ = 168.3; 167.3 |
| | S $2p_{1/2}$ | $C \times 0.5$ | $F \times 1.1$ | $I + 1.1$ |
| $S^{2-}$ ($MoS_2$/$K_2MoS_4$)[d] | S 2s | $(1.5 \times A)/1.7$; $(1.5 \times A)/1.4$ | $D \times 1.5$ | $(G + 65)$; $(G + 64)$ |
| $S^{2-}$ (K–$Mo^{IV}$(S)) | S 2s | $(1.5 \times B)/1.7$; $(1.5 \times B)/1.4$ | $E \times 1.5$ | $(H + 65)$; $(H + 64)$ |
| $SO_4^{2-}$ | S 2s | $(1.5 \times C)/1.7$; $(1.5 \times C)/1.4$ | $F \times 1.5$ | $(I + 65)$; $(I + 64)$ |
| $Mo^{IV}$ ($MoS_2$) | Mo $3d_{5/2}$ | $J$ | $M = \text{fwhm}_{\text{Al 2p}} \times \beta$[a] | P = 229.5; 228.8 |
| | Mo $3d_{3/2}$ | $J \times 0.67$ | $M \times 1.05$ | $P + 3.15$ |
| $Mo^{IV}$ (K–$Mo^{IV}$(S)) | Mo $3d_{5/2}$ | $K$ | $N = \text{fwhm}_{\text{Al 2p}} \times \varepsilon$[a] | $Q$ = 228.6; 227.8 |
| | Mo $3d_{3/2}$ | $K \times 0.67$ | $N \times 1.05$ | $Q + 3.15$ |
| $Mo^{VI}$ ($K_2MoS_4$) | Mo $3d_{5/2}$ | $L$ | $O = \text{fwhm}_{\text{Al 2p}} \times \theta$[a] | $R$ = 230.4; 229.8 |
| | Mo $3d_{3/2}$ | $L \times 0.67$ | $O \times 1.05$ | $R + 3.15$ |

[a] The fwhm constraints ($D$ and $M$–$O$) regarding S $2p_{3/2}$ and Mo $3d_{5/2}$ were obtained from experimental data using the fwhm of $Al_{2p}$. $\alpha = 0.9 \pm 0.1$; $\beta = 0.8 \pm 0.2$; $\varepsilon = 0.6 \pm 0.2$; $\theta = 0.7 \pm 0.2$ [b] E.g. "$G$ = 162.1; 161.1" means that the value of the BE can evolve during the fit between 161.1 and 162.1 eV. [c] For $Na_2MoO_4$/Al, just replace K by Na in this column. [d] It was experimentally shown (e.g., see Figure 4) that the S $2p_{3/2}$ and S 2s peaks due to $K_2MoS_4$ supported on alumina are observed in the same regions (162–161 eV and 226–225 eV, respectively) as the S $2p_{3/2}$ and S 2s peaks due to $MoS_2$. Thus, the peaks due to these two entities were both simulated by one component.

Table 7. Binding Energies and Relative Atom % of Mo Species in Activated Catalysts

| | Mo $3d_{5/2}$ binding energy (eV) | | | rel atom % of Mo species (%$Mo_i$) | | |
|---|---|---|---|---|---|---|
| catalyst | $Mo^{IV}$(S) | $Mo^{V}$(O–S) | $Mo^{VI}$(O) | $Mo^{IV}$(S) | $Mo^{V}$(O–S) | $Mo^{VI}$(O) |
| Mo/Al | 228.9 | 230.4 | 232.6 | 72 | 12 | 16 |
| | Mo $3d_{5/2}$ binding energy (eV) | | | rel atom % of Mo species (%$Mo_i$) | | |
| | K–$Mo^{IV}$(S) | $Mo^{IV}$(S) | $Mo^{VI}$(O) | K–$Mo^{IV}$(S) | $Mo^{IV}$(S) | $Mo^{VI}$(O) |
| K+Mo/Al | 228.4 | 229.4 | 232.9 | 41 | 49 | 10 |
| | Mo $3d_{5/2}$ binding energy (eV) | | | rel atom % of Mo species (%$Mo_i$) | | |
| | K(Na)–$Mo^{IV}$(S) | $Mo^{IV}$(S) | $Mo^{VI}$(S) | K(Na)–$Mo^{IV}$(S) | $Mo^{IV}$(S) | $Mo^{VI}$(S) |
| $Na_2MoO_4$/Al | 228.4 | 229.2 | 230.2 | 48 | 43 | 9 |
| $K_2MoO_4$/Al | 228.2 | 229.1 | 230.0 | 48 | 38 | 14 |
| $K_2MoS_4$/Al | 228.3 | 229.1 | 230.0 | 61 | 22 | 17 |

making it impossible to differentiate the pure $MoS_2$ phase and that decorated by $K^+$ using XRD characterization. The disproportionation of COS and subsequent hydrogenation of $CS_2$ to form $CH_3SH$ was then assigned to the CUS sites of the $K^+$-decorated $MoS_2$ phase.

On the other hand, it is very well known that molybdenum disulfide ($MoS_2$) features a layered structure, in which the atoms are covalently bonded to form two-dimensional layers that are stacked together through weak van der Waals interactions. The weak interlayer interaction allows foreign ions or molecules to be introduced between the layers through intercalation. In this regard, numerous works have been reported concerning the intercalation of ions or molecules into the structure of $MoS_2$ layers, and among those, the intercalation of lithium has been widely discussed, mainly due to its application as electrode materials for batteries with high energy storage.[53−58] The intercalation of an alkali metal such as lithium into $MoS_2$ layers ($Li_xMoS_2$) may be described as an ion–electron transfer reaction. The electrons from the lithium (guest) are transferred to the unoccupied energy levels of the $MoS_2$ (host), which are mainly transition-metal d bands.[55] However, the intercalation actually may also induce important structural changes in the host at a high amount of alkali metal. Upon intercalation, the local coordination geometry of the Mo centers of the host lattice changes from trigonal prismatic (2H-$MoS_2$, equivalent to the classical active phase for hydrotreatment catalysts) to distorted octahedral (1T-$MoS_2$). This 2H to 1T phase transition is accompanied by considerable changes in the band structure and an increased electron density on the molybdenum atoms of the $MoS_2$ lattice.[59,60] Thus, the induced electronics and structural changes of $MoS_2$ by the incorporation of Li have been studied by X-ray photoelectron spectroscopy. XPS results obtained by Papageorgopoulos et al.[56] performed on a Li intercalated $MoS_2$ single crystal showed a shift toward lower binding energies of Mo 3d core levels of about 1.1 eV, which was explained by the 2H to 1T phase transition.[55,56] In this study, metallic lithium was deposited under UHV at room temperature onto the basal $MoS_2$ planes (0001), corresponding to the intercalation process across the van der Waals planes. Intercalation proceeded through Li electron transfer to the d orbitals of Mo in order to accept a $Li^+$ between the layers. In a different approach of preparing alkali metal intercalated $MoS_2$, $K_xMoS_2$ was also prepared.[59,61] The synthesis consists of the sulfidation of $K_2MoO_4$ with $H_2S$ at 400 °C to give $K_2MoS_4$, followed by reduction under $H_2$ at high temperature (800 °C), leading to metallic $K_xMoS_2$ with a structure related to 2H-

$MoS_2$. By low temperature water treatment, a partial oxidation of the sulfide phase together with hydration of the $K^+$ cations is observed to form $K_x(H_2O)_yMoS_2$. From studies on a single crystal (hydrated) of $K_xMoS_2$, Wypych et al.[60,61] suggest that, in contrast to the case for 2H-$MoS_2$, every Mo center in this compound is octahedrally surrounded by six sulfur ligands (1T-$MoS_2$), whereas the hydrated $K^+$ cations are located in the van der Waals gap between the layers.

The octahedral structure [$MoS_6$] of this species depends largely on the amount of potassium located between the layers. Thus, if the number of $K^+$ cations in the van der Waals gap decreases, the stabilization of the octahedral Mo coordination becomes less effective and an increased tendency for a reorientation to the trigonal-prismatic coordination mode can be observed.

On the basis of the literature data about the formation of the $K_xMoS_2$ intercalated phase and taking into account the results obtained by XPS by Papageorgopoulos[56] on a Li intercalated $MoS_2$ compound, we propose that for K(Na)Mo activated catalysts the Mo $3d_{5/2}$ component positioned at 228.3 eV (±0.1 eV) is due to the formation of a $K(Na)_xMoS_2$ intercalated phase corresponding to the $MoS_2$ phase with K(Na) cations intercalated between the $MoS_2$ layers (called K(Na)−$Mo^{IV}$ in the section 3.3.1). In our study, the formation of $K_xMoS_2$ with $K^+$ intercalated cations could be explained by the presence of potassium in a large quantity, which induces the formation of 1T-$MoS_2$. This latter phase can be reduced under hydrogen; this reduction (visible by the Mo 3d XPS shift of around 1 eV) facilitates the insertion of $K^+$ cations for charge equilibrium. To our knowledge, this is the first time that such a phase has been put in evidence by XPS on K(Na)Mo supported sulfide catalysts.

The formation of a $K_xMoS_2$ intercalated phase was also supported by the decomposition of the S 2p photopeak. Table 8 displays the resulting binding energies of the S $2p_{3/2}$ peaks related to the different species identified after sulfidation of the catalysts.

**Table 8. Binding Energies of Sulfur Species of Activated Catalysts**

| catalyst | binding energy (eV) of S $2p_{3/2}$: $S^{2-}$ | $(S-S)^{2-}$ |
|---|---|---|
| Mo/Al | 161.7 | 162.7 |

| catalyst | binding energy (eV) of S $2p_{3/2}$: $S^{2-}$ ($MoS_2$) | $S^{2-}$ ($K_xMoS_2$) | $SO_4^{2-}$ |
|---|---|---|---|
| K+Mo/Al | 161.8 | 163.4 | 168.1 |

| catalyst | binding energy (eV) of S $2p_{3/2}$: $S^{2-}$ ($MoS_2$/$K_2MoS_4$) | $S^{2-}$ ($K_xMoS_2$) | $SO_4^{2-}$ |
|---|---|---|---|
| $Na_2MoO_4$/Al | 161.7 | 163.4 | 167.8 |
| $K_2MoO_4$/Al | 161.6 | 163.3 | 168.0 |
| $K_2MoS_4$/Al | 161.6 | 163.3 | 167.7 |

For Mo/Al, the two components of the S 2s core level at 162.7 and 161.7 eV were assigned to disulfide bridges $(S-S)^{2-}$ and sulfide $S^{2-}$ ligands, respectively. The latter component is consistent with the $S^{2-}$ type ligands present in $MoS_2$, whereas $(S-S)^{2-}$ entities are present in oxysulfide compounds containing $Mo^V$ species, in agreement with the two components obtained from the decomposition of XPS S 2s core level shown in Figure 7. Different S 2p spectra were observed for K-promoted catalysts, for which it was not possible to decompose correctly the main peaks of these spectra using the same components as those used for Mo/Al. Thus, the decomposition of the S 2p spectrum displays three different components, which are in agreement with the three components proposed for the decomposition of XPS S 2s core level in the corresponding Mo 3d−S 2s spectrum shown in Figure 7. The first component at 161.6 ± 0.1 eV is identified for both nonpromoted and K-promoted solids and assigned to $S^{2-}$ species present in $MoS_2$. A second component at higher binding energy (168.0 ± 0.1 eV) is detected for K-promoted catalysts. This component is attributed to the presence of sulfate species ($SO_4^{2-}$), in agreement with literature data.[40] A third and new component at 163.3 ± 0.1 eV appears on the K-promoted catalysts. This component obviously cannot be related to $(S-S)^{2-}$species as observed in Mo/Al at 162.7 eV, since the Mo 3d decomposition of K-containing catalysts does not reveal the presence of oxysulfide species ($Mo^V$) correlated to a $(S-S)^{2-}$contribution. Papageorgopoulos[56] reported that Li deposition between $MoS_2$ layers caused a shift of the S 2p photoemission peak to higher BE and that further increase of Li deposition cause a broadening of the S 2p peak which may be fitted by two independent components separated by 0.8 eV. We observed the widening of the S 2p peak after introduction of potassium (sodium) and also an important shift (1.7 eV) toward higher binding energies. We propose that this sulfur component with unusual binding energy is also linked to the presence of $K(Na)_xMoS_2$ intercalated species. Thus, this sulfur component around 163.3 eV is another evidence of the $K(Na)_xMoS_2$ intercalated phase formation in the K(Na)-containing catalysts. It is then assumed, taking into account literature data, that the specific 1T $MoS_2$ crystallographic phase presenting electron density variation for both S and Mo species (in comparison to the classical 2H $MoS_2$ phase) is stabilized by the presence of a high quantity of $K^+$ cations forming the $K_xMoS_2$ intercalated phase. Moreover, the K 2p binding energy of the potassium-containing catalysts after sulfidation (Figure S4 in the Supporting Information) corresponds clearly to that of $K^+$ cations without an energy shift, indicating the preservation of $K^+$ species in the intercalated $K_xMoS_2$ phase.

### *3.3.3. Laser Raman Spectroscopy of Activated Catalysts.*

Figure 9 displays the Raman spectra of activated $K_2MoO_4$/$Al_2O_3$ and $K_2MoS_4$/$Al_2O_3$ catalysts. Both spectra look very similar, with two main lines at 376 and 400 $cm^{-1}$, respectively,

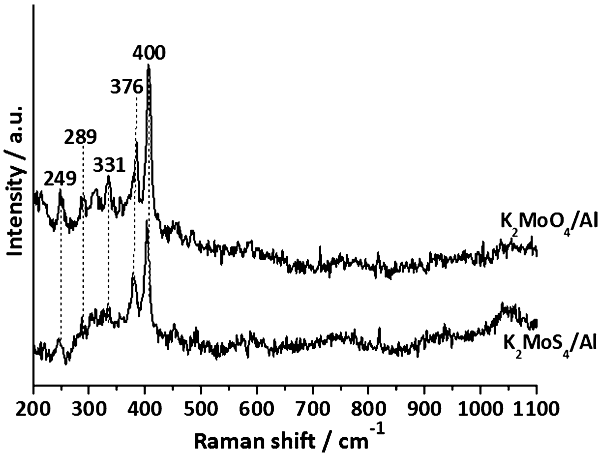

**Figure 9.** Raman spectra of $K_2MoO_4$/Al and $K_2MoS_4$/Al activated catalysts.

Table 9. Determination of Mo Atoms Charged in the Reactor and Detected by XPS ($n_{Mo}$)

| catalyst | catalyst density (g mL$^{-1}$) | $m_{Mo}$(reactor) (g) | $n_{Mo}$(reactor) | %Mo detected by XPS | $n_{Mo}$ |
|---|---|---|---|---|---|
| Mo/Al | 0.48 | 1.152 | $7.2 \times 10^{21}$ | 71 | $5.2 \times 10^{21}$ |
| Mo+K/Al | 0.53 | 1.264 | $7.9 \times 10^{21}$ | 38 | $3.0 \times 10^{21}$ |
| $Na_2MoO_4$/Al | 0.49 | 1.184 | $7.4 \times 10^{21}$ | 32 | $2.4 \times 10^{21}$ |
| $K_2MoO_4$/Al | 0.52 | 1.256 | $7.9 \times 10^{21}$ | 29 | $2.3 \times 10^{21}$ |
| $K_2MoS_4$/Al | 0.63 | 1.512 | $9.5 \times 10^{21}$ | 16 | $1.6 \times 10^{21}$ |

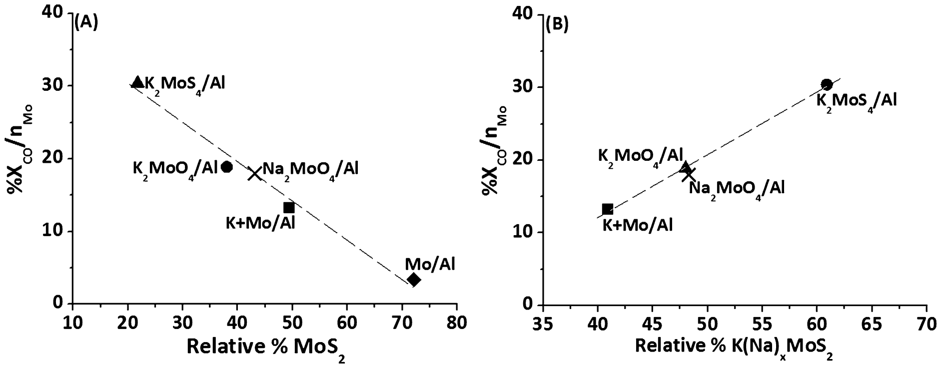

**Figure 10.** Correlation between CO conversion per Mo atom charged in the reactor and detected by XPS and relative percentages of $MoS_2$ (A) and $K_xMoS_2$ (B) phases in activated catalysts. Reaction conditions: 320 °C, 10 bar, 1333 h$^{-1}$, CO/$H_2$/$H_2S$ = 1/2/1.

assigned to Mo−S and S−Mo−S stretching modes.[31,62−64] The observation of both lines is related to the formation of the classical 2H-$MoS_2$ phase, as already reported for sulfided Mo/$Al_2O_3$ HDS catalyst.[63,64] In addition to these two main lines, Raman lines are observed at lower wavenumbers around 249 and 331 cm$^{-1}$. It has been reported by Voiry et al.[65] that upon lithium intercalation inducing the transformation of the trigonal-prismatic $MoS_2$ phase (2H phase) into the phase corresponding to an octahedral coordination (1T phase) of Mo atoms, deep modifications in the Raman are observed. New Raman peaks have then been identified at low wavenumbers such as ∼160, 230, and 330 cm$^{-1}$ for the 1T-$MoS_2$ prepared using $LiBH_4$.[65] These new Raman peaks are explained by new vibration modes allowed for the 1T-$MoS_2$ phase. The results achieved from the Raman analysis of activated catalysts are in agreement with the formation of the intercalated phase 1T-$MoS_2$ resulting from the insertion of $K^+$ between the $MoS_2$ layers.

*3.3.4. Correlation between Catalytic Performances and the Intercalated $K_xMoS_2$ Phase.* The careful decomposition of Mo 3d XPS spectra allowed obtaining the relative atom % of each corresponding Mo species (%Mo$_i$) according to the formula

$$\%Mo_i = [A_i(Mo3d_{3/2} + Mo3d_{5/2})/ \sum (A_i(Mo3d_{3/2} + Mo3d_{5/2}))] \times 100$$

where $A_i$(Mo 3d$_{3/2}$ + Mo 3d$_{5/2}$) is the area of one Mo component.

The relative atomic percent (%Mo$_i$) of each solid is reported in Table 7. For the nonpromoted catalyst Mo/Al the predominant phase (over 70%) is $MoS_2$, while $Mo^V$ oxysulfide and $Mo^{VI}$ oxospecies represent the minority. In the K(Na)-promoted solids, various relative amounts of the $K_xMoS_2$ phase were found: in K+Mo/Al, 41% of the Mo corresponds to the $K_xMoS_2$ phase, while for K(Na)$_2$MoO$_4$- and $K_2MoS_4$-based catalysts, the major phase was $K_xMoS_2$ with relative amounts of 48% and 61%, respectively.

The Mo distributions cannot be directly compared to the catalytic performances. Indeed, for catalysts before activation it was previously seen by XPS that the Mo dispersion strongly differs for the different types of solids (see Table 2). Thus, the %Mo detected by XPS was also calculated for catalysts after activation and the values are reported in Table 2. For all catalysts, sulfidation led to a decrease in the %Mo detected by XPS, suggesting sintering and formation of larger particles after activation. The presence of these large particles was confirmed when the corresponding samples were analyzed using transmission electron microscopy. Actually, these particles can be observed on many TEM images obtained on activated K−Mo catalysts. Accordingly, Mo/Al was still the best dispersed solid after activation, whereas on K(Na)Mo-based solids, a very low dispersion was observed (only 16% of Mo detected by XPS in $K_2MoS_4$/Al). This behavior can also be observed in Figure 3. The open symbols are representative of activated catalysts. Thus, we observed that, in comparison to catalysts, the activated catalysts exhibited a more significant deviation from the Kerkhof−Moulijn model, highlighting the fact that the sulfidation step led to a decrease in the %Mo detected by XPS. in agreement with the agglomeration of the molybdenum species on the surface of the support after sulfidation.

By analogy with studies on sulfide hydrotreating catalysts where activities are well-correlated to the CoMoS active phase detected by XPS, we considered as possible active species the Mo species detected by XPS in $MoS_2$ and $K_xMoS_2$ phases, whereas larger particles not detected by XPS were thought to be inactive. This point has to be taken into account before any correlation with the catalytic performances can be made. Moreover, in the reactor was introduced 30 mL of catalyst, which corresponds to different catalyst weights, since the densities of all of the solids are not equivalent, and as a consequence, different amounts of Mo were really introduced in the reactor ($n_{Mo}$(reactor)). Thus, considering all these parameters, the real quantity of Mo atoms introduced in the reactor and detected by XPS ($n_{Mo}$) was calculated for each catalyst and reported in Table 9.

The CO conversion per Mo atom charged in the reactor and detected by XPS ($\%X_{CO}/n_{Mo}$) was plotted against the relative percentages of $MoS_2$ and $K(Na)_xMoS_2$. The obtained plots are displayed in Figure 10. Methyl mercaptan productivity per Mo atom charged in the reactor and detected by XPS as a function of the relative percent of $K(Na)_xMoS_2$ is reported in Figure 11.

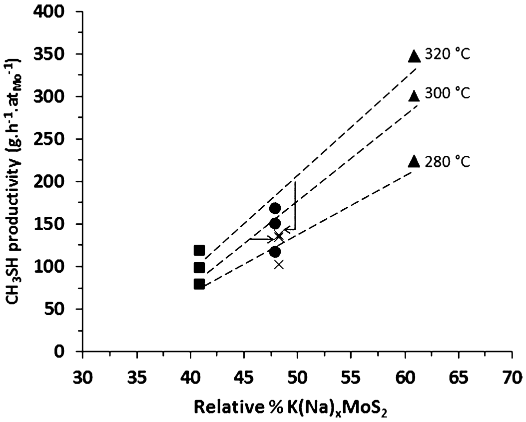

**Figure 11.** Correlation between $CH_3SH$ productivity per Mo atom charged in the reactor and detected by XPS and relative precentages of $K_xMoS_2$ phase: (■) K+Mo/Al; (●) $K_2MoO_4$/Al; (×) $Na_2MoO_4$/Al; (▲) $K_2MoS_4$/Al. Reaction conditions: 320 °C, 10 bar, 1333 $h^{-1}$, CO/$H_2$/$H_2S$ = 1/2/1.

Figure 10A shows the CO conversion ($\%X_{CO}/n_{Mo}$) as a function of the relative percentage of the $MoS_2$ phase. There is an inverse correlation between $\%X_{CO}/n_{Mo}$ values of all catalysts and the relative percentage of the $MoS_2$ phase. In fact, the higher the $MoS_2$ relative percentage, the lower the CO conversion, highlighting the fact that the formation of this phase cannot explain the K-promoted catalyst performances. As shown in Figure 10B, the opposite behavior is observed when $\%X_{CO}/n_{Mo}$ is plotted against the relative percentage of the $K(Na)_xMoS_2$ phase. Actually, the higher the relative percentage of the $K(Na)_xMoS_2$ phase, the higher the CO conversion. These results suggest that CO conversion is governed by the amount of K(Na) intercalated $MoS_2$ phase.

A good correlation is also observed when plotting the $CH_3SH$ productivity per Mo atom charged in the reactor and detected by XPS against the relative percentage of the $K(Na)_xMoS_2$ phase (see Figure 11). Indeed, $CH_3SH$ productivity increases linearly with the amount of $K_xMoS_2$ for K-promoted catalysts. The presence of $K_xMoS_2$ species is required to reach higher CO conversion and also higher $CH_3SH$ selectivity. On the basis of these statements, intercalated $K_xMoS_2$ is proposed to be the active phase for methyl mercaptan synthesis from CO/$H_2$/$H_2S$.

*3.3.4. High-Resolution Transmission Electron Microscopy (HRTEM).* With the aim of determining the morphology of the active phase, activated catalysts were analyzed using high-resolution transmission electron microscopy (HRTEM). As examples, typical HRTEM images of Mo/Al and low-loaded (8.1 %Mo) and high-loaded (17.9 %Mo) $K_2MoO_4$/Al activated

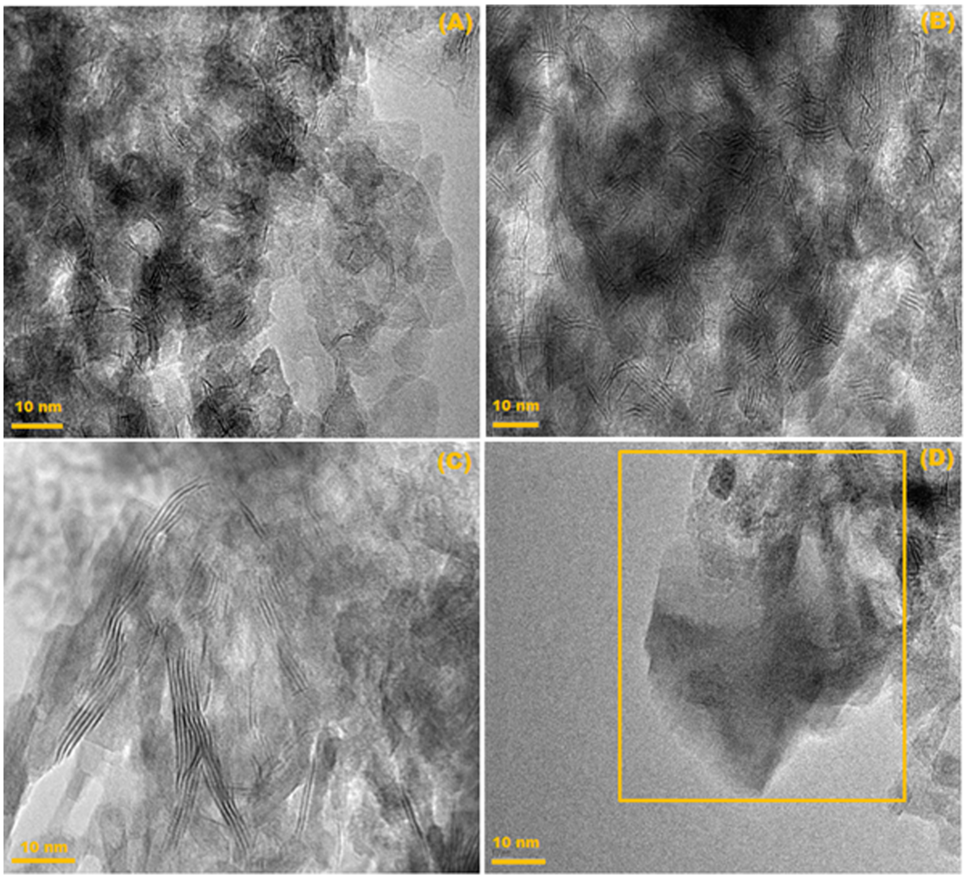

**Figure 12.** High-resolution TEM images of activated catalysts, (A) Mo/Al; (B) $K_2MoO_4$/Al; (C) high-loaded $K_2MoO_4$/Al; (D) $K_2MoO_4$/Al (large particles).

catalysts are shown in Figure 12. The micrographs display the presence of $MoS_2$ layers in the three analyzed samples. Images of the Mo/Al sample (A) exhibit poorly stacked bent $MoS_2$ slabs. In the $K_2MoO_4$/Al sample (B), at first sight TEM images do not allow discriminating between $MoS_2$ and the active $K_xMoS_2$ phase, but it is evidenced that the $MoS_2$ slabs of these K-containing catalysts are apparently longer with higher stacking.

A statistical analysis of these samples was carried out in order to determine the average slab length and the average stacking degree. For Mo/Al, the average slab length was 2.9 nm with a stacking degree equal to 1.5. For the low-loaded $K_2MoO_4$/Al these values were 4.9 and 2.5 nm, respectively, suggesting an effect of potassium on the slab length and stacking degree due to its intercalated position between the $MoS_2$ slabs. Such increases could appear as a drawback, considering the preparation of highly active HDS catalysts whose catalytic activity is mostly due to the edges of the $MoS_2$ slabs. However, for $CH_3SH$ synthesis by reaction of syngas and hydrogen sulfide, at this stage of the study, the location of the active sites is still unknown. Thus, no conclusion should be made at this point before more information is available on the location of these catalytically active sites. A TEM image of the high-loaded (17.9%) activated $K_2MoO_4$/Al catalyst (Figure 12C) has been chosen to more clearly show the unusual morphology of the $MoS_2$ phase. This solid exhibits very long slabs (average length 9 nm) and high stacking between 1 and 9 with an average value of 2.7. Thus, when the K and Mo loading is increased in these solids, the size and stacking of $MoS_2$ slabs significantly increase. This behavior is clearly different in comparison to highly loaded supported (Co)Mo/$Al_2O_3$ HDS catalyst, on which so long and stacked $MoS_2$ slabs are not observed. Indeed, after sulfidation of these CoMo catalysts, mainly single and bilayered slabs with length around 3 nm are usually observed.[66,67] Thus, the active phase morphology observed on the high-loaded $K_2MoO_4$/Al catalyst confirms the results obtained on the low-loaded solids. Nevertheless, it has been reported by Afanasiev[53] that the sulfidation/decomposition of bulk ammonium thiomolybdate ($(NH_4)_2MoS_4$) under $H_2$/$H_2S$ leads to a typical thiomolybdate decomposition product constituted by stacks of four to seven slabs having length 5−8 nm. Moreover, we already observed that the sulfidation of crystalline species (such as $MoO_3$) with low interaction with the support led to highly stacked and long $MoS_2$ particles around a $MoO_3$ core, leading to bulk poorly sulfided $MoO_3$ crystallites.[68] It could be thought that the very long and stacked $MoS_2$ slabs that we observed in activated KMo supported catalysts could originate from the sulfidation of large particles whose presence has been deduced from Raman spectroscopy (narrow Raman lines) and from XPS analysis (indicating a low dispersion of Mo for the $K_2MoS_4$/Al, $K_2MoO_4$/Al, and K+Mo/Al solids). Such large particles are visible on TEM images, as shown in Figure 12D. Nevertheless, if sulfidation of large particles leads to long and stacked $MoS_2$ slabs, the amount of Mo detected by XPS is expected to increase after sulfidation (because large particles in which Mo cannot be detected by XPS are transformed into slabs in which Mo should be detected), which is not observed, as reported in Table 2. Furthermore, if the $MoS_2$ slab length and stacking originate from the presence of large particles, a higher Mo content in $K_2MoO_4$-based catalysts should not modify the $MoS_2$ slab morphology; in our study we detected a modification of $MoS_2$ slab morphology. It can be then assumed that this unusual morphology of the $MoS_2$ phase in K−Mo catalysts can be ascribed to the formation of very large and stacked $MoS_2$ crystallites with intercalated K ions stabilizing the 1T-$MoS_2$ phase.

## 4. CONCLUSION

From the evaluation of catalytic performances, the simultaneous presence of potassium and molybdenum into the catalytic system is a key factor to achieve higher CO conversion and higher $CH_3SH$ selectivity and productivity along with a low $CO_2$ selectivity. The incorporation of K and Mo coming from a unique precursor was beneficial in terms of catalytic performance but also with regard to the time and cost of preparation of catalysts. It was remarkable that using potassium leads to a higher $CH_3SH$ selectivity and a lower $CO_2$ selectivity than is the case using sodium as a promoter. An extensive and careful study by XPS allowed us to propose an intercalated $K_xMoS_2$ phase as the active phase of activated KMo-based catalysts. In this intercalated $K_xMoS_2$ phase, the Mo 3d binding energy is shifted toward a lower value from 229.4 eV (2H-$MoS_2$) to 228.4 eV, suggesting the stabilization of the 1T-$MoS_2$ phase obtained through potassium cation interaction. Correlations have been obtained between the relative amount of $K_xMoS_2$ and (i) CO conversion and (ii) $CH_3SH$ productivity, taking into account the quantity of molybdenum detected by XPS. The HRTEM study of sulfided catalysts showed that the presence of potassium increased the slab length and stacking degree of $MoS_2$ slabs. This unusual morphology can be attributed to the potassium intercalation into the $MoS_2$ phase.

## ■ ASSOCIATED CONTENT

### Ⓢ Supporting Information

The following file is available free of charge on the ACS Publications website at DOI: 10.1021/cs502031f.

> Characterization of the $K_2MoS_4$ precursor by laser Raman and UV−visible spectroscopy, XPS spectra of the Mo 3d level of catalysts Mo/Al, K+Mo/Al, $K_2MoO_4$/Al, and $Na_2MoO_4$/Al, and K 2p photopeaks of catalysts and activated catalysts (PDF)

## ■ AUTHOR INFORMATION

### Corresponding Author

*C.L.: fax, +33 (0) 3 20 43 65 61; tel, +33 (0)3 20 43 49 50; e-mail, carole.lamonier@univ-lille1.fr.

### Notes

The authors declare no competing financial interest.

## ■ ACKNOWLEDGMENTS

The authors gratefully acknowledge Patrice Barre and Karine Sanchou from the “Groupement de Recherches de Lacq” GRL (ARKEMA) for catalytic testing. The research leading to all the results included in this work has received funding from the European Union Seventh Framework Programme (FP7/2007−2013) under grant agreement No. 241718 EuroBioRef. The TEM facility in Lille, France, is supported by the Conseil Regional du Nord-Pas de Calais and the European Regional Development Fund (ERDF).

## ■ REFERENCES

(1) Leuchtenberger, W.; Huthmacher, K.; Drauz, K. *Appl. Microbiol. Biotechnol.* **2005**, *69*, 1−8.

(2) Gomes, J.; Kumar, D. *Enzyme Microb. Technol.* **2005**, *37*, 3−18.

(3) Devaux, J.-F.; Dubois, J.-L. US Patent 2011/0229626 A1, 2011.

(4) Gillete, L. US Patent 3299146, 1967.
(5) Arretz, E. US Patent 5312993, 1994.
(6) Finšgar, M.; Milošev, I. *Corros. Sci.* **2010**, *52*, 2430−2438.
(7) Stinn, D. E.; Swindell, H. J.; Kubicek, D. H.; Johnson, M. M. US Patent 5898012, 1999.
(8) Doumani, T. F. US Patent 3006966, 1961.
(9) Doumani, T. F. US Patent 2829171, 1958.
(10) Kramer, R. L.; Reid, E. E. *J. Am. Chem. Soc.* **1921**, *43*, 880−890.
(11) Folkins, H. O. US Patent 2786079, 1957.
(12) Mul, G.; Wachs, I. E.; Hirschon, A. S. *Catal. Today* **2003**, *78*, 327−337.
(13) Zhang, B.; Taylor, S. H.; Hutchings, G. J. *New J. Chem.* **2004**, *28*, 471−476.
(14) Zhang, B.; Taylor, S. H.; Hutchings, G. J. *Catal. Lett.* **2003**, *91*, 181−183.
(15) Yang, Y.-Q.; Yuan, Y.-Z.; Dai, S.-J.; Wang, B.; Zhang, H.-B. *Catal. Lett.* **1998**, *54*, 65−68.
(16) Dai, S.; Yang, Y.-Q.; Yuan, Y.; Tang, D.; Lin, R.; Zhang, H. *Catal. Lett.* **1999**, *61*, 157−160.
(17) Yang, Y.-Q.; Wang, Q.; Lin, R.; Zhang, H.-B.; Yuan, Y.-Z.; Fang, W.; Zheng, Q.; Dai, S.-jun; Yan, X.; Chen, A.; Barth, J.-olaf; Weckbecker, C.; Huthmacher, K.; Ackermann, S. WO Patent 2005/040082 A2 2005.
(18) Chen, A. P.; Wang, Q.; Hao, Y. J.; Fang, W. P.; Yang, Y.-Q. *Catal. Lett.* **2008**, *121*, 260−265.
(19) Chen, A.; Wang, Q.; Li, Q.; Hao, Y.; Fang, W.; Yang, Y.-Q. *J. Mol. Catal. A: Chem.* **2008**, *283*, 69−76.
(20) Gutierrez, O. Y.; Kaufmann, C.; Lercher, J. A. *ACS Catal.* **2011**, *1*, 1595−1603.
(21) Yang, Y.-Q.; Dai, S.; Yuan, Y.; Lin, R.; Tang, D.; Zhang, H. *Appl. Catal., A* **2000**, *192*, 175−180.
(22) Gutiérrez, O. Y.; Kaufmann, C.; Hrabar, A.; Zhu, Y.; Lercher, J. A. *J. Catal.* **2011**, *280*, 264−273.
(23) Moses, P. G.; Hinnemann, B.; Topsøe, H.; Nørskov, J. K. *J. Catal.* **2009**, *268*, 201−208.
(24) Gutiérrez, O. Y.; Kaufmann, C.; Lercher, J. A. *ChemCatChem* **2011**, *3*, 1480−1490.
(25) Gutiérrez, O. Y.; Zhong, L.; Zhu, Y.; Lercher, J. A. *ChemCatChem* **2013**, *5*, 3249−3259.
(26) Harmer, M. A.; Sykes, G. *Inorg. Chem.* **1980**, *19*, 2881−2885.
(27) Carrier, X.; Lambert, J. F.; Che, M. *J. Am. Chem. Soc.* **1997**, *119*, 10137−10146.
(28) Le Bihan, L.; Blanchard, P.; Fournier, M.; Grimblot, J.; Payen, E. *J. Chem. Soc., Faraday Trans.* **1998**, *94*, 937−940.
(29) Blanchard, P.; Lamonier, C.; Griboval, a.; Payen, E. *Appl. Catal., A* **2007**, *322*, 33−45.
(30) Murugan, R.; Huang, P. J.; Ghule, A.; Chang, H. *Thermochim. Acta* **2000**, *346*, 83−90.
(31) Hao, Y.; Zhang, Y.; Chen, A.; Fang, W.; Yang, Y.-Q. *Catal. Lett.* **2009**, *129*, 486−492.
(32) Pérez-Martínez, D. J.; Eloy, P.; Gaigneaux, E. M.; Giraldo, S. A.; Centeno, A. *Appl. Catal., A* **2010**, *390*, 59−70.
(33) La Parola, V.; Deganello, G.; Tewell, C. R.; Venezia, A. M. *Appl. Catal., A* **2002**, *235*, 171−180.
(34) Erdöhelyi, A.; Fodor, K.; Solymosi, F. *J. Catal.* **1997**, *166*, 244−253.
(35) Herrera, J. E.; Resasco, D. E. *J. Catal.* **2004**, *221*, 354−364.
(36) Mahadevan Pillai, V. P.; Pradeep, T.; Bushiri, M. J.; Jayasree, R. S.; Nayar, V. U. *Spectrochim. Acta, Part A* **1997**, *53*, 867−876.
(37) Müller, A.; Baran, E. J.; Carter, R. O. Vibrational spectra of oxo-, thio-, and selenometallates of transition elements in the solid state. In *Spectra and Chemical Interactions. Structure and Bonding*; Springer: Berlin Heidelberg, 1976; Vol. *26*, pp 81−139.
(38) Müller, A.; Weinstock, N.; Schulze, H. *Spectrochim. Acta* **1972**, *28A*, 1075−1082.
(39) Weber, T.; Muijsers, J. C.; W, N. J. *J. Phys. Chem.* **1995**, *99*, 9194−9200.
(40) Qiu, L.; Xu, G. *Appl. Surf. Sci.* **2010**, *256*, 3413−3417.
(41) Roukoss, C.; Laurenti, D.; Devers, E.; Marchand, K.; Massin, L.; Vrinat, M. *C. R. Chim.* **2009**, *12*, 683−691.
(42) Wang, H. W.; Skelton, P.; Thompon, G. E. *Surf. Coat. Technol.* **1997**, *91*, 200−207.
(43) Kerkhof, F. P. J. M.; Moulijn, J. A. *J. Phys. Chem.* **1979**, *83*, 1612−1619.
(44) Boulinguiez, M.; Forquy, C.; Barrault, J. US Patent 4665242, 1987.
(45) Haines, P. G. US Patent 4449006, 1984.
(46) Olin, J. F.; Buchholz, B.; Goshorn, R. H. US Patent 3070632, 1962.
(47) Barth, J.-olaf; Redlingshöfer, H.; Weckbecker, C.; Huthmacher, K.; Zanthoff, H.-W.; Mayer, R. European Patent 1982764 A1 2008.
(48) Barrault, J.; Boulinguiez, M.; Forquy, C.; Maurel, R. *Appl. Catal.* **1987**, *33*, 309−330.
(49) Faraji, F.; Safarik, I.; Strausz, O. P.; Torres, M. E.; Yildirim, E. *Ind. Eng. Chem. Res.* **1996**, *35*, 3854−3860.
(50) Alstrup, I.; Chorkendorff, I.; Candia, R.; Clausen, B.; Topsøe, H. *J. Catal.* **1982**, *77*, 397−409.
(51) Nielsen, L. P.; Schonning, M.; Christensen, S.; Hoffmann, S.; Li, Z.; Hofmann, P.; Besenbacher, F.; Clausen, B. *Catal. Lett.* **2001**, *73*, 85−90.
(52) Gandubert, A. D.; Legens, C.; Guillaume, D.; Rebours, S.; Payen, E. *Oil Gas Sci. Technol.* **2007**, *62*, 79−89.
(53) Afanasiev, P. *C. R. Chim.* **2008**, *11*, 159−182.
(54) Julien, C. M. *Mater. Sci. Eng., R* **2003**, *40*, 47−102.
(55) Benavente, E.; Santa Ana, M. A.; Mendizabal, F.; Gonzalez, G. *Coord. Chem. Rev.* **2002**, *224*, 87−109.
(56) Papageorgopoulos, C. A.; Jaegermann, W. *Surf. Sci.* **1995**, *338*, 83−93.
(57) Enyashin, A. N.; Seifert, G. *Comput. Theor. Chem.* **2012**, *999*, 13−20.
(58) Feng, C.; Ma, J.; Li, H.; Zeng, R.; Guo, Z.; Liu, H. *Mater. Res. Bull.* **2009**, *44*, 1811−1815.
(59) Wypych, F.; Weber, T.; Prins, R. *Surf. Sci.* **1997**, *380*, L474−L478.
(60) Wypych, F.; Weber, T.; Prins, R. *Chem. Mater.* **1998**, *10*, 723−727.
(61) Wypych, F.; Schollhorn, R. *J. Chem. Soc., Chem. Commun.* **1992**, *19*, 1386−1388.
(62) Viršek, M.; Jesih, A.; Milošević, I.; Damnjanović, M.; Remškar, M. *Surf. Sci.* **2007**, *601*, 2868−2872.
(63) Payen, E.; Kasztelan, S.; Grimblot, J. *J. Mol. Struct.* **1988**, *174*, 71−76.
(64) Schrader, G. L.; Cheng, C. P. *J. Catal.* **1983**, *80*, 369−385.
(65) Voiry, D.; Salehi, M.; Silva, R.; Fujita, T.; Chen, M.; Asefa, T.; Shenoy, V. B.; Eda, G.; Chhowalla, M. *Nano Lett.* **2013**, *13*, 6222−6227.
(66) Frizi, N.; Blanchard, P.; Payen, E.; Baranek, P.; Dupuy, C.; Rebeilleau, M.; Dath, J. P. *Catal. Today* **2008**, *130*, 272−282.
(67) Eijsbouts, S.; Van Den Oelelaar, L. C. A.; Van Puijenbroek, R. R. *J. Catal.* **2005**, *229*, 352−364.
(68) Lamonier, C.; Martin, C.; Mazurelle, J.; Harlé, V.; Guillaume, D.; Payen, E. *Appl. Catal., B* **2007**, *70*, 548−556.